

Fast Inverse Nonlinear Fourier Transforms for Continuous Spectra of Zakharov-Shabat Type

Sander Wahls, *Member, IEEE* and Vishal Vaibhav

Abstract—The nonlinear Schrödinger equation (NSE) is well-known to model an ideal fiber-optic communication channel. Even though the NSE is a nonlinear evolution equation, it can be solved analytically using a nonlinear Fourier transform (NFT). Recently, there has been much interest in transceiver concepts that utilize this NFT and its inverse to (de-)modulate data. Fast algorithms for the (inverse) NFT are a key requirement for the simulation and real-time implementation of fiber-optic communication systems based on NFTs. While much progress has already been made for accelerating the forward NFT, less is known on its inverse. The nonlinear Fourier spectrum comprises a continuous and a discrete part in general, but so far only fast inverse NFTs for signals whose continuous spectrum is null have been reported in the literature. In this paper, we investigate the complementary case and propose the first fast inverse NFT for signals whose discrete spectrum is empty. This is the case required by transmitters in the recently proposed nonlinear inverse synthesis scheme, but the problem also occurs in different application areas such as fiber Bragg grating design. Our algorithms require only $\mathcal{O}(D \log^2 D)$ floating point operations to generate D samples of the desired signal, which is almost an order of magnitude faster than the current state of the art, $\mathcal{O}(D^2)$. This paper also quantifies, apparently for the first time, the impact that truncating a signal in the time-domain has on the NFT.

Index Terms—Nonlinear Fourier transform, Optical fiber communication, Signal processing algorithms

I. INTRODUCTION

The *nonlinear Fourier transform (NFT)* of Zakharov and Shabat [1] transforms a (Lebesgue-measurable) signal

$$q : \mathbb{R} \rightarrow \mathbb{C}, \quad \exists c, d > 0 \text{ s.t. } |q(t)| \leq ce^{-2d|t|}, \quad (1)$$

from the time- into the nonlinear Fourier domain by using it as a symbol in the linear ordinary differential equation

$$\frac{d}{dt}\phi = \begin{bmatrix} j\lambda & q(t) \\ -\kappa\bar{q}(t) & -j\lambda \end{bmatrix} \phi, \quad \phi = \begin{bmatrix} \phi_1(t, \lambda) \\ \phi_2(t, \lambda) \end{bmatrix}, \quad (2)$$

subject to the initial condition

$$\lim_{t \rightarrow -\infty} e^{j\lambda t} \phi(t, \lambda) = \begin{bmatrix} 1 \\ 0 \end{bmatrix}. \quad (3)$$

Here, λ is a fixed complex parameter, the overbar denotes the complex conjugate, j is the imaginary number, and \mathbb{R} and \mathbb{C} denote the real and complex numbers, respectively. The significance of the parameter $\kappa \in \{\pm 1\}$ will be discussed

shortly. The boundary condition (3) fixes ϕ at $t \rightarrow -\infty$. The behavior of ϕ for $t \rightarrow +\infty$ is determined through $q(t)$. It can be assessed using the normalized limits

$$\alpha(\lambda) := \lim_{t \rightarrow +\infty} e^{j\lambda t} \phi_1(t, \lambda), \quad \beta(\lambda) := \lim_{t \rightarrow +\infty} e^{-j\lambda t} \phi_2(t, \lambda). \quad (4)$$

The NFT of $q(t)$ is defined in terms of these limits. It consists, in general, of the following two parts:

- 1) The *continuous spectrum*¹

$$\hat{q}(\lambda) = \frac{\beta(\lambda)}{\alpha(\lambda)}, \quad \lambda \in \mathbb{R}. \quad (5)$$

- 2) The *discrete spectrum*

$$(\zeta_k, \tilde{q}_k)_{k=1}^K,$$

where the *eigenvalues* ζ_k are the solutions to

$$\alpha(\zeta_k) = 0, \quad \Im\{\zeta_k\} > 0, \quad (6)$$

and the *residuals* satisfy

$$\tilde{q}_k := \beta(\zeta_k) / \frac{d\alpha}{d\lambda}(\zeta_k), \quad (7)$$

assuming that the eigenvalues are simple roots of $\alpha(\lambda)$.

An *inverse NFT* accepts a nonlinear Fourier spectrum consisting of a continuous part and a discrete part as defined above, and then computes the corresponding signal $q(t)$ that generates this spectrum. This is visualized below,

$$\hat{q}(\lambda), \quad (\zeta_k, \tilde{q}_k)_{k=1}^K \xrightarrow{\text{Inverse NFT}} q(t).$$

Inverse NFTs have recently appeared as a computationally intensive part of several newly proposed transceiver architectures in fiber-optic communications. Before we discuss these in more detail, we remark in passing that the inversion of the Zakharov-Shabat NFT is a fundamental problem that arises in many other areas of science and engineering such as *fiber Bragg grating design* [2], *nuclear magnetic resonance* [3], [4], *quantum field theory* [5], *transmission line models* [6], and, in its discrete form, *seismic inversion* [7].

Let us now discuss the relation between the NFT and fiber-optic communication. The spatial evolution of a fiber-input in an ideal single-mode fiber simplifies greatly in the nonlinear Fourier domain such that it can be solved in closed form. Let $u(x, t)$ denote the complex envelope of the

¹Another common designation is *reflection coefficient*. The eigenvalues defined in (6) are also known as *bound states*, while the residuals in (7) are sometimes called *spectral amplitudes* in the literature.

Both authors are with the Delft University of Technology, Delft Center for Systems and Control, Delft, The Netherlands, e-mail: s.wahls@tudelft.nl, v.k.vaibhav@tudelft.nl.

electrical field in an ideal fiber, whose evolution is described through the *nonlinear Schrödinger equation* [8, Ch. 3.3]

$$j\frac{\partial u}{\partial x} + \frac{\partial^2 u}{\partial t^2} + 2\kappa|u|^2u = 0. \quad (8)$$

Here, $x \geq 0$ denotes the location in the fiber and t denotes retarded time. The parameter κ determines if the dispersion in the fiber is normal (-1) or anomalous ($+1$). (Note that this is the normalized form of the nonlinear Schrödinger equation, in which the fiber parameters have been absorbed by rescaling q , x and t .) We denote the NFT of the complex envelope $u(x_0, t)$ at a fixed location $x = x_0$ by $\hat{u}(x_0, \lambda)$, $\zeta_k(x_0)$ and $\tilde{u}_k(x_0)$, where $k = 1, \dots, K(x_0)$. The spatial evolution of the envelope $u(x, t)$, which has no explicit solution in the time-domain, reduces to a few simple multiplications in the nonlinear Fourier domain [9, p. 261]:

$$\begin{aligned} \hat{u}(x_0, \lambda) &= \hat{u}(0, \lambda)e^{-4j\lambda^2x_0}, & \zeta_k(x_0) &= \zeta_k(0), \\ \tilde{u}_k(x_0) &= \tilde{u}_k(0)e^{-4j\zeta_k^2(0)x_0}, & K(x_0) &= K(0). \end{aligned}$$

Nonlinear effects are now a major limiting factor in fiber-optic communications [10]. The prospect of treating them using simple closed-form formulas has recently spurred much research activity on how NFTs may be utilized to transmit information [11], [12], [13], [14], [15], [16], [17], even though the basic idea was already proposed in 1993 by Hasegawa and Nyu [18]. The principal feasibility of these ideas has now been demonstrated in several experiments [19], [20], [21], [22], even though the spectral efficiencies of these systems are currently low compared to those achieved by conventional state-of-the-art systems that are the results of decades of engineering.

The computational complexity of the NFT and inverse NFT operations however poses a significant problem for the investigation of these concepts, both in simulations and experiments. While the numerical complexity of the forward NFT has been reduced quite significantly during the few last years [23], [24], [25], less has been achieved so far for the inverse NFT. The goal of inverse NFT algorithms is to generate a prespecified number – say, D – of samples of the time-domain signal $q(t)$ that corresponds to a specified nonlinear Fourier spectrum. The complexity of an inverse NFT algorithm is typically measured in the order of the number of *floating points operations (flops)* that is required to compute these samples. Recently, two fast algorithms that can compute the inverse NFT for the special case of purely discrete spectra (i.e., $\hat{q}(\lambda) = 0$ for all real λ) have been presented [26], [27]. The algorithm in [26] requires only $\mathcal{O}(D \log^2 D)$ flops, but has the disadvantage that only the eigenvalues, but not the residuals can be controlled. The algorithm in [27] requires $\mathcal{O}(KD + D \log^2 D)$ flops, where K is the number of eigenvalues in the discrete spectrum, and offers control over both the eigenvalues and the residuals. However, no fast inverse NFT algorithms are so far available for purely continuous spectra.

In this paper, we will close this gap and derive the first fast inverse NFT algorithms for purely continuous spectra. In other words, we assume that the discrete part of the

nonlinear Fourier spectrum that is provided to the inverse NFT is empty, $K = 0$. Whenever the constant κ in (2) is negative, this actually means no loss of generality because no discrete spectrum can form in this case anyway. The case of negative κ occurs whenever fiber-optic communication over a defocusing fiber is considered, as is the case e.g. in [12], [16], [28]. The fastest currently known algorithms require $\mathcal{O}(D^2)$ flops to generate D samples [29]. Given that the number of samples is often high (e.g., $D = 16384$ in [28]), the computational costs even of these algorithms will be significant. We remark that the inverse NFT for $\kappa = -1$ also describes the fiber Bragg grating design problem, where the number of samples can be as high as $D = 262144$ in astronomical applications [29]. The case of positive κ in (2) corresponds to fiber-optic communication over a focusing fiber. The *nonlinear inverse synthesis (NIS)* method of Prilepsky et al. [13], [14], [30], [22], [31] utilizes only the continuous part of the nonlinear Fourier spectrum, and therefore could profit directly from the algorithms proposed in this paper as they allow to reduce the complexity of the transmitter significantly. This is especially interesting as it was already demonstrated in [32] that the receiver complexity of the NIS scheme can be significantly reduced by using fast forward NFTs without any loss of performance (in terms of Q -factor). Combining these results would result in a NFT-based transceiver with an overall $\mathcal{O}(D \log^2 D)$ complexity, which is close to conventional OFDM systems.²

The paper is structured as follows. In the next section, we rederive and analyze commonly used discretizations of the NFT. (The analysis includes new results.) Then, in Section III, we present two new fast inverse NFT algorithms based on this discretization. The first algorithm will aim at the defocusing case $\kappa = -1$ [cf. (2)], while the second algorithm will aim at the focusing case $\kappa = +1$. In Section IV, the merits of our new algorithms are investigated in numerical examples. We compare their performance in terms of both speed, error and robustness against high degrees of nonlinearity with several existing methods from the literature. Finally, the paper is concluded in Section V.

II. DISCRETIZATION OF THE NFT

In this section, we discuss how the continuous-time NFT (5)–(7) can be discretized such that it becomes amenable to computation. The discretizations presented in the following are well-known, but we nevertheless present some derivations here to make clear how our problem statement, which is formulated in a discrete-time framework, is related to the original continuous-time formulation. We remark that our derivations are somewhat different in that we utilize the Magnus expansion [33, Sec. 5]. This allows us to avoid the usual ad hoc assumption that $q(t)$ is piecewise constant, whose impact on the numerical error has mostly been neglected in the literature related to NFTs so far.³ We

²The investigation of this accelerated NIS scheme was regrettably beyond the scope of this paper, but we plan to investigate it in the future.

³The paper [34] by Burtsev et al. is the only exception we are aware of.

also quantify, apparently for the first time, the error that results from assuming that the signal has a finite support.

During the numerical computations, the initial condition (3) at minus infinity will be replaced with

$$e^{j\lambda T_1} \phi(T_1) = \begin{bmatrix} 1 \\ 0 \end{bmatrix}, \quad (9)$$

where T_1 is “close” to $-\infty$. Similarly, the limits in the definitions of $\alpha(\lambda)$ and $\beta(\lambda)$ in (4) are replaced with

$$\tilde{\alpha}(\lambda) := e^{j\lambda T_2} \phi_1(T_2, \lambda), \quad \tilde{\beta}(\lambda) := e^{-j\lambda T_2} \phi_2(T_2, \lambda), \quad (10)$$

where T_2 is “close” to $+\infty$. These replacements are exact whenever the to be transformed signal $q(t)$ is zero outside the interval $[T_1, T_2]$. However, practically relevant signals like the soliton do not satisfy this assumption. It is therefore desirable to bound the error due to these approximations. The following theorem provides such a bound.

Theorem 1. Fix an arbitrary δ in the open interval $(0, 1)$. We denote the $\tilde{\alpha}(\lambda)$ and $\tilde{\beta}(\lambda)$ that correspond to the choice

$$[T_1, T_2] = [T_0 - m\delta, T_0 + m\delta], \quad m = 1, 2, \dots, \quad (11)$$

by $\tilde{\alpha}^m(\lambda)$ and $\tilde{\beta}^m(\lambda)$, respectively. Also fix an arbitrary $d_0 \in (0, d)$, where d is the rate of decay in (1). Then, for any λ such that $0 \leq \Im\lambda \leq d_0 < d$, the sequences $\tilde{\alpha}^m(\lambda)$ and $\tilde{\beta}^m(\lambda)$, $m = 1, 2, \dots$; converge with (finite) limits $\alpha(\lambda)$ and $\beta(\lambda)$, respectively. The truncation error satisfies

$$\left\| \begin{bmatrix} \alpha(\lambda) \\ \beta(\lambda) \end{bmatrix} - \begin{bmatrix} \tilde{\alpha}^m(\lambda) \\ \tilde{\beta}^m(\lambda) \end{bmatrix} \right\| = \mathcal{O}(e^{-2(d-d_0)\delta m}), \quad (12)$$

where the hidden constant in the big- \mathcal{O} symbol depends on c , d , d_0 , T_0 and δ , but not on λ or m ; the norm is Euclidean.

As we could not find this result in the literature, a proof is presented in the appendix. A few remarks are in order.

Remark 2. Even though the ansatz of replacing $-\infty$ with T_1 and $+\infty$ with T_2 is widely used for the numerical computation of the NFT, we have not been able to find a theoretical validation of this seemingly straight-forward approach in the literature. Theorem 1 not only shows that the estimates converge, but that they converge towards the correct values. It therefore finally provides a theoretical fundament for many numerical methods to compute the NFT.

Remark 3. The constant $\delta < 1$ should be interpreted as a sampling interval, which makes $2m - 1$ the number of samples used in a discretization. Sampling intervals larger than one can be accommodated by scaling the time axis [11, p. 4319]. Note that this changes the rate of decay d .

Remark 4. The region $0 \leq \Im\lambda < d$ is consistent with the results in [9, p. 268]; for a signal decaying as in (1), the functions $\alpha(\lambda)$ and $\beta(\lambda)$ are analytic in this region.

In light of Theorem 1, we neglect the truncation error from now on with the implicit understanding that $[T_1, T_2]$ is large enough. Next, we derive several iterative formulas that allow us to approximate $\phi(T_2)$ numerically, and discuss how these formulas can be used to approximate the NFT.

A. Magnus Integrator

In order to discretize (2), we first define the grid of points

$$t_n := T_1 + n\varepsilon, \quad \varepsilon := \frac{T_2 - T_1}{D}, \quad n = 0, 1, \dots, D. \quad (13)$$

The evolution of ϕ in (2) over one subinterval $[t_n, t_{n+1}]$ is given by the following analytic formula,

$$\phi(t_{n+1}) = e^{\Omega_n(t_{n+1})} \phi(t_n), \quad (14)$$

where $e^{\mathbf{X}}$ denotes the matrix exponential and $\Omega_n(t) = \sum_{k=1}^{\infty} \Omega_{n,k}(t)$ is a so-called *Magnus expansion*, assuming that the interval length $\varepsilon = t_{n+1} - t_n$ is small enough [35, p. 119]. The first term of the Magnus expansion is given by

$$\Omega_{n,1}(t) = \int_{t_n}^t \mathbf{A}(\tau) d\tau, \quad \mathbf{A}(\tau) := \begin{bmatrix} j\lambda & q(\tau) \\ -\kappa\bar{q}(\tau) & -j\lambda \end{bmatrix}.$$

We only retain this first term of the Magnus expansion and apply the mid-point rule to discretize it. The result reads

$$\tilde{\phi}(t_{n+1}) = e^{\varepsilon \mathbf{A}_n} \tilde{\phi}(t_n), \quad \mathbf{A}_n := \mathbf{A}\left(\frac{t_n + t_{n+1}}{2}\right). \quad (15)$$

The total error induced by truncating the Magnus expansion and discretizing the first term is of order $\mathcal{O}(\varepsilon^3)$ given that $\mathbf{A}(\tau)$ is sufficiently regular in the interval $[t_n, t_{n+1}]$ [35, Def. I.1.2+Exa. IV.7.3]. We remark that, in the context of NFTs, the discretization (15) is due to Boffetta and Osborne [36, Eq. 4.2]. Essentially the same discretization has also been derived earlier by Yamada and Sakuda [37] in the context of fiber Bragg gratings. Similar methods furthermore appear in earlier papers on other scattering problems, such as [38], [39]. Boffetta and Osborne actually cite Magnus’ work, but they apply it under the assumption that $q(t)$ is constant on each interval $[t_n, t_{n+1}]$. The only paper that analyzes the implicit error induced by a piecewise constant assumption in the context of NFTs is, to the best of our knowledge, the paper of Burtsev et al. [34, Sec. 4.1].

B. Split Magnus Integrator

The matrix exponential in the discretization (15) can be difficult to compute [40]. We therefore introduce matrices

$$\mathbf{B}_n := \begin{bmatrix} j\lambda & 0 \\ 0 & -j\lambda \end{bmatrix}, \quad \mathbf{C}_n := \begin{bmatrix} 0 & q_n \\ -\kappa\bar{q}_n & 0 \end{bmatrix},$$

where the q_n denote the mid-point values

$$q_n := q\left(\frac{t_n + t_{n+1}}{2}\right), \quad (16)$$

and apply a symmetric Strang splitting [35, p. 42],

$$e^{\varepsilon \mathbf{A}_n} = e^{\varepsilon \mathbf{B}_n/2} e^{\varepsilon \mathbf{C}_n} e^{\varepsilon \mathbf{B}_n/2} + \mathcal{O}(\varepsilon^3). \quad (17)$$

With $z := e^{2j\lambda\varepsilon}$, the matrix $e^{\varepsilon \mathbf{B}_n/2}$ can be written as

$$e^{\varepsilon \mathbf{B}_n/2} = \begin{bmatrix} e^{j\lambda\varepsilon/2} & 0 \\ 0 & e^{-j\lambda\varepsilon/2} \end{bmatrix} = \begin{bmatrix} z^{1/4} & 0 \\ 0 & z^{-1/4} \end{bmatrix}. \quad (18)$$

The matrix $e^{\varepsilon C_n}$ can also be simplified. We apply results in [41] and find that, whenever $\Delta := \sqrt{-\kappa\varepsilon|q_n|} \neq 0$,

$$\begin{aligned} e^{\varepsilon C_n} &= \begin{bmatrix} \cosh(\Delta) & \varepsilon q_n \frac{\sinh(\Delta)}{\Delta} \\ -\kappa\varepsilon\bar{q}_n \frac{\sinh(\Delta)}{\Delta} & \cosh(\Delta) \end{bmatrix} \\ &= \begin{bmatrix} \cosh(\Delta) & \frac{e^{j\angle q_n}}{\sqrt{-\kappa}} \sinh(\Delta) \\ \sqrt{-\kappa\varepsilon} e^{-j\angle q_n} \sinh(\Delta) & \cosh(\Delta) \end{bmatrix}. \end{aligned} \quad (19)$$

The second line, (19), can be shown to hold also in the trivial case $\Delta = 0$. We simplify (19) further using the expressions

$$\begin{aligned} \cosh(\Delta) &= \frac{1}{\operatorname{sech}(\Delta)} = \frac{1}{\sqrt{1 - \tanh^2(\Delta)}} \\ &= \frac{1}{\sqrt{1 - \Delta^2}} + \mathcal{O}(\Delta^3), \end{aligned} \quad (20)$$

$$\begin{aligned} \sinh(\Delta) &= \Delta \cosh(\Delta) + \mathcal{O}(\Delta^3) \\ &= \frac{\Delta}{\sqrt{1 - \Delta^2}} + \mathcal{O}(\Delta^3), \end{aligned} \quad (21)$$

which both stem from Taylor's theorem. [Note that (20) was used to derive (21).] Applying (20) and (21) in (19) leads to

$$e^{\varepsilon C_n} = \frac{1}{\sqrt{1 - \Delta^2}} \begin{bmatrix} 1 & \varepsilon q_n \\ -\kappa\varepsilon\bar{q}_n & 1 \end{bmatrix} + \mathcal{O}(\varepsilon^3). \quad (22)$$

Finally, after plugging (18) and (22) into (17), we arrive at

$$e^{\varepsilon A_n} = \frac{1}{\sqrt{1 - \Delta^2}} \begin{bmatrix} z^{\frac{1}{2}} & \varepsilon q_n \\ -\kappa\varepsilon\bar{q}_n & z^{-\frac{1}{2}} \end{bmatrix} + \mathcal{O}(\varepsilon^3).$$

We now obtain a second discretization of the analytical formula (14) by replacing $e^{\varepsilon A_n}$ in the discretization (15):

$$\check{\phi}(t_{n+1}) = \frac{1}{\sqrt{1 + \kappa|\varepsilon q_n|^2}} \begin{bmatrix} z^{\frac{1}{2}} & \varepsilon q_n \\ -\kappa\varepsilon\bar{q}_n & z^{-\frac{1}{2}} \end{bmatrix} \check{\phi}(t_n). \quad (23)$$

This discretization is, except for the square root factor, due to Ablowitz and Ladik [42]. We remark that the numerical accuracy drops to first order without the factor. While this is not an issue when computing forward NFTs – the square factor cancels out in that case – it is important to keep the factor in our case as we will be working directly with the discretized wave functions. The idea to include the square root factor seems to be due to Newell [43, p. 449f, Ref. 13]. The splitting (17), but not the simplification of the hyperbolic terms, has also been proposed by Fedec et al. [44, Eq. 16].

C. Split Magnus Integrator with Transformed Coordinates

We apply the following change of coordinates to (23),

$$\mathring{\phi}(t) := \begin{bmatrix} 1 & 0 \\ 0 & z^{\frac{1}{2}} \end{bmatrix} \check{\phi}(t), \quad (24)$$

which leads to the equivalent discretization

$$\mathring{\phi}(t_{n+1}) = \frac{z^{-\frac{1}{2}}}{\sqrt{1 + \kappa|\varepsilon q_n|^2}} \begin{bmatrix} 1 & \varepsilon q_n z^{-1} \\ -\kappa\varepsilon\bar{q}_n & z^{-1} \end{bmatrix} \mathring{\phi}(t_n). \quad (25)$$

This discretization is very close to a discretization of Skaar et al. [2, p. 166], for which εq_n has to be replaced with $\tanh(\varepsilon|q_n|)e^{j\angle q_n}$ [2, Eq. 4]. The difference is of third order.

D. Numerical Computation of the Continuous-Time NFT

In principle, any of the three discretizations just derived can be used to compute numerical approximations of the functions $\alpha(\lambda)$ and $\beta(\lambda)$ that are used to define the NFT. The split Magnus integrator with changed coordinates, for example, leads to the approximations

$$\hat{\alpha}(\lambda) := e^{j\lambda T_2} \mathring{\phi}_1(t_D), \quad \hat{\beta}(\lambda) := e^{-j\lambda T_2} z^{-\frac{1}{2}} \mathring{\phi}_2(t_D), \quad (26)$$

where $\mathring{\phi}_1$ and $\mathring{\phi}_2$ denote the components of the vector $\mathring{\phi}$, and the factor $z^{-\frac{1}{2}}$ arises because of the change of coordinates in (24). To find $\mathring{\phi}(t_D)$ for any fixed λ , the initial condition $\mathring{\phi}(t_0) = \phi(T_1)$ as given in (9) is iterated using (25).

The split Magnus discretizations given above interestingly do not only provide a discretization of the continuous-time NFT, but leads to discrete-time NFTs in their own right that operate on discrete-time signals [45], [46]. Furthermore, these discrete-time NFTs can be accelerated similar to how the conventional *fast Fourier transform (FFT)* accelerates the discrete-time Fourier transform [23], [24]. The plain Magnus discretization does not enjoy these advantages.

In the remainder of this paper, we will rely on the split Magnus integrator with transformed coordinates given in (25). It will be useful to normalize (25) as follows,

$$\begin{aligned} \begin{bmatrix} A_{n+1}(z) \\ B_{n+1}(z) \end{bmatrix} &= \frac{1}{\sqrt{1 + \kappa|Q[n]|^2}} \begin{bmatrix} 1 & Q[n]z^{-1} \\ -\kappa\bar{Q}[n] & z^{-1} \end{bmatrix} \\ &\quad \times \begin{bmatrix} A_n(z) \\ B_n(z) \end{bmatrix}, \end{aligned} \quad (27)$$

$$\begin{bmatrix} A_0(z) \\ B_0(z) \end{bmatrix} = \begin{bmatrix} 1 \\ 0 \end{bmatrix}, \quad n = 0, 1, \dots, D-1, \quad (28)$$

where the normalized samples $Q[n]$ are given by

$$Q[n] := \varepsilon q_n = \varepsilon q \left(\frac{t_n + t_{n+1}}{2} \right). \quad (29)$$

The normalized and the original discretization are related as

$$\mathring{\phi}_1(t_n) = e^{-j\lambda T_1} z^{-\frac{n}{2}} A_n, \quad \mathring{\phi}_2(t_n) = e^{-j\lambda T_1} z^{-\frac{n}{2}} B_n, \quad (30)$$

where the exponential stems from the initial condition (9) and the factor $z^{-\frac{n}{2}}$ arises because we dropped the factor $z^{\frac{1}{2}}$ above the square root in (25) in (27).

E. Discrete-Time NFT

The normalized discretization (27)–(28) leads to the following discrete-time version of the NFT, where we focus our attention on finite-length signals, and use the short-hands

$$A(z) := A_D(z), \quad B(z) := B_D(z)$$

to simplify the notation. The *discrete-time NFT* of any finite-length signal $Q[n]$, $n = 0, 1, \dots, D-1$, consists of

1) The *continuous spectrum*

$$\hat{Q}(z) := \frac{B(z)}{A(z)}, \quad |z| = 1. \quad (31)$$

2) The *discrete spectrum*

$$(\xi_k, \tilde{Q}_k)_{k=1}^K,$$

where the *eigenvalues* ξ_k are the solutions to

$$A(\xi_k) = 0, \quad |\xi_k| > 1,$$

and the *residuals* are given by

$$\tilde{Q}_k = B(\xi_k) / \frac{dA}{dz}(\xi_k),$$

assuming that the eigenvalues are simple roots.

The relation between the continuous-time NFT of a signal $q(t)$ and the discrete-time NFT of the discrete-time signal $Q[n]$ given in (29) can be examined using the results derived so far. The continuous spectra are related as

$$\begin{aligned} \hat{q}(\lambda) &= \frac{\beta(\lambda)}{\alpha(\lambda)} && \stackrel{(26)}{\approx} e^{-j\lambda(2T_2)} z^{-\frac{1}{2}} \frac{\hat{\phi}_2(t_D)}{\hat{\phi}_1(t_D)} \\ & && \stackrel{(13),(30)}{=} e^{-j\lambda(T_2+T_1+D\varepsilon)} z^{-\frac{1}{2}} \frac{B(z)}{A(z)}, \\ & && \stackrel{\text{Def. } z}{=} e^{-j\lambda(T_2+T_1)} z^{-\frac{D+1}{2}} \hat{Q}(z). \end{aligned} \quad (32)$$

Similar formulas exist for the discrete spectrum, but we skip these as our focus is on signals with empty discrete spectra.

III. FAST INVERSE NONLINEAR FOURIER TRANSFORM

In this paper, we are concerned with computing inverse NFTs. While the inverse NFT has already been discussed in the introduction for continuous time, we now consider its numerical implementation. Remember that we only consider signals with empty discrete spectra. In this setting, an inverse NFT algorithm is typically provided samples of the desired continuous spectrum, and uses them to compute samples of the corresponding time-domain signal:

$$\text{Samples of } \hat{q}(\lambda) \xrightarrow[\text{Inverse NFT}]{\text{Numerical}} \text{Samples of } q(t). \quad (33)$$

In the literature, two main approaches can be found. The first approach is to solve the *Gelfand-Levitan-Marchenko (GLM) equations*, which are coupled integral equations, numerically [1], [47]. Recently developed algorithms based on the GLM equations are able to recover D such samples using $\mathcal{O}(D^2)$ floating point algorithms (*flops*) with an approximation error that has been observed to decrease quadratically [48]. The second approach is layer peeling. Discrete-time layer peeling algorithms, which have been found to be superior to continuous-time variants [2], [28], start by reconstructing q_{D-1} from a specified discrete reflection coefficient $\hat{Q}(z)$. Then, a discretized version of the Zakharov-Shabat equation such as (27) is used to find the reflection coefficient that corresponds the same discrete-time signal, but with $q_{D-1} = 0$, effectively reducing the length of the signal. The process is repeated until all samples q_n have been reconstructed. Layer peeling algorithms can be implemented using $\mathcal{O}(D^2)$ flops as well [34], with an error that has also been observed to vanishes quadratically. *Integral layer peeling* combines both approaches by first splitting the continuous-time signal $q(t)$ into segments, which are then discretized by applying the GLM equations locally [49]. The *Riccati equation* approach, in which a Riccati equation that describes the evolution of

ϕ_2/ϕ_1 is utilized, can also be implemented with $\mathcal{O}(D^2)$ flops [50]. We are not aware of any algorithm that solves the inverse NFT problem (33) with less than $\mathcal{O}(D^2)$ flops.

The two fast $\mathcal{O}(D \log^2 D)$ algorithms we are going to present now are thus the first of their kind. Both are layer peeling methods that proceed in two steps. The provided reflection coefficient is first used to synthesize suitable wave functions, $A(z)$ and $B(z)$, via interpolation [46], after which the samples are recovered using layer peeling:

$$\hat{q}(\lambda) \xrightarrow[\hat{Q}(z_k)=\sigma_k]{\text{Interpolation}} A(z), B(z) \xrightarrow{\text{Layer peeling}} q_n.$$

In order to achieve our goal of a fast algorithm, both steps must be carried using $\mathcal{O}(D \log^2 D)$ flops. The layer peeling step can be made fast using a method developed by McClary for seismic inversion [51], as has recently been demonstrated in [26], [16]. We will not discuss this part further.

The novel aspect of our fast algorithms lies in how we synthesize the wave functions $A(z)$ and $B(z)$ that serve as the input for the layer peeling step. The main difficulty is that the wave functions cannot be chosen arbitrarily. In practice, one always considers a finite number D of samples in the discretized problem (27). It follows via induction that

$$A(z) = \sum_{k=0}^{D-1} A_k z^{-k} \text{ and } B(z) = \sum_{k=0}^{D-1} B_k z^{-k} \quad (34)$$

have to be polynomials of degree $D - 1$. Since layer peeling is based on inverting (27), there should exist samples q_0, q_1, \dots, q_{D-1} that, when plugged into (27), actually lead to the generated wave functions. Otherwise, the task of recovering such samples is ill-posed, and the layer peeling step may suffer from numerical instabilities. Skaar and his coworkers have coined the term *realizability* for this issue [52], [53]. They showed that the wave functions in (34) can be generated through (27) for a suitable choice of samples q_0, q_1, \dots, q_{D-1} if and only if the three conditions

$$|A(z)|^2 + \kappa|B(z)|^2 = 1 \text{ whenever } |z| = 1, \quad (35)$$

$$A(z) \neq 0 \text{ whenever } |z| > 1 \text{ and } z \notin \{\xi_k\}, \quad (36)$$

$$A_0 \text{ is real and non-negative} \quad (37)$$

are satisfied. (The same results have also been found in [54], [55].) We remark that many layer peeling algorithms work directly with the reflection coefficient instead of the wave functions. The issue of realizability however remains also in this case because not all reflection coefficients correspond to a finite-length grating with the desired length.

Existing layer peeling methods are not adequately taking realizability into account. They either completely ignore the fact that the generated grating has to be of finite length [44], [2], [56], [57], or they do not ensure that the resulting discrete-time realizability conditions (35)–(37) are satisfied [52], [28]. Instead, the corresponding continuous-time realizability conditions are used to determine the continuous-time wave functions $\alpha(\lambda)$ and $\beta(\lambda)$, and the discrete-time wave functions $A(z)$ and $B(z)$ are found by approximating

Algorithm 1 Prototype for the fast inverse NFTs

- Input:** Reflection coefficient $\hat{q}(\lambda)$, support $[T_1, T_2] \ni t$ of $q(t)$, number of samples D
- Output:** Samples q_n as defined in (16) s.t. $\hat{Q}(z)$ given in (31) satisfies the interpolation conditions (38)
- 1) *Synthesis:* Construct $A(z)$ and $B(z)$ such that $\hat{Q}(z)$ is a “good” approximation of $\hat{q}(\lambda)$ w.r.t. (32).
 - 2) *Layer peeling:* Recover the samples q_n from $A(z)$ and $B(z)$ using fast layer peeling as in [51], [26].
-

them using (26) and (30), or similar relations. The synthesized discrete-time wave functions usually still satisfy (35)–(37) approximately, but not exactly. The mismatch to realizability can be interpreted as measurement noise. Since layer peeling is known to be sensitive against measurement noise, especially for strong gratings [58], the applicability of conventional layer peeling methods is limited by this issue.

Algorithm 1 shows the prototype for our fast inverse nonlinear Fourier transforms. Both algorithms use, as was already mentioned before, the fast layer peeling method of McClary [51], [26]. The *synthesis step* will however be different, as is explained below. Note that McClary himself mentioned that his algorithm is unstable in the presence of measurement noise. However, in our context measurement noise is equivalent to violating the realizability conditions. Therefore, we will focus especially on fulfilling them during synthesis.

A. Outline of Synthesis via Interpolation

In this paper, the synthesis step of finding suitable wave functions that will serve as inputs for the layer peeling step is based on solving the interpolation problem (see [46])

$$\frac{B(z_n)}{A(z_n)} = \sigma_n, \quad n = 0, 1, \dots, D-1, \quad (38)$$

where the target values are, in light of (31)–(32), given by

$$\sigma_n := e^{j\lambda_n(T_2+T_1)} z^{\frac{D+1}{2}} \hat{q}(\lambda_n).$$

The interpolation nodes $z_n := e^{2j\lambda_n \varepsilon}$ are chosen equidistantly on the unit circle such that the value $z = -1$, which is ambiguous under the transform $z = e^{2j\lambda \varepsilon}$, is avoided:

$$\lambda_n := -\frac{\delta}{2} + \left(n + \frac{1}{2}\right) \frac{\delta}{D}, \quad \delta := \frac{\pi}{\varepsilon} = \frac{\pi D}{T_2 - T_1}. \quad (39)$$

In other words, the discrete-time continuous spectrum $\hat{Q}(z)$ is supposed to match the continuous-time specification $\hat{q}(\lambda)$ on the frequency grid $\{\lambda_n\}$. Summarizing, our goal is thus to generate wave functions of the form (34) that solve the interpolation problem (38) and, in light of the discussion above, satisfy the three realizability conditions (35)–(37).

Remark 5. Due to discretization errors and mismatches at frequencies that are not on the grid, fulfilling the interpolation conditions does not guarantee an exact match with the desired continuous-time reflection coefficient.

An important insight arises when the realizability condition (35) is combined with the definition of $\hat{Q}(z)$ in (31):

$$|A(z)|^2 = 1 - \kappa|B(z)|^2 = 1 - \kappa|\hat{Q}(z)|^2|A(z)|^2.$$

Solving for $|A(z)|^2$, one finds that

$$|A(z)|^2 = \frac{1}{1 + \kappa|\hat{Q}(z)|^2}, \quad |z| = 1. \quad (40)$$

Note that due to the realizability condition (37) and our assumption that the discrete spectrum is empty, $A(z)$ has no roots outside the unit disc. Therefore, we can recover $A(z)$ by spectral factorization of (40) [59].

B. First Algorithm: Iterative Synthesis

While solving the interpolation problem (38) subject to the realizability conditions (35)–(37) is difficult in general, solving the closely related interpolation problem

$$\frac{B(z_n)}{|A(z_n)|} = \sigma_n, \quad n = 0, 1, \dots, D-1, \quad (41)$$

subject to realizability has an explicit solution [46, IV.B]. The polynomial $B(z)$ in this solution is determined though

$$B(z_n) = \frac{\sigma_n}{\sqrt{1 + \kappa|\sigma_n|^2}}, \quad n = 0, 1, \dots, D-1. \quad (42)$$

The corresponding $A(z)$ is found via spectral factorization of $|A(z)|^2 = 1 - \kappa|B(z)|^2$. When the polynomials $A(z)$ and $B(z)$ that solve (41) are evaluated in the actual interpolation problem (38), one finds that the magnitudes match, but the phases are incorrect. Our idea is thus to iteratively solve simple interpolation problems of the form (41) while adapting the phases such that the phase mismatch is reduced more and more. We start by initializing auxiliary interpolation targets $\sigma'_n := \sigma_n$, and iterate the following steps several times.

- 1) Find the polynomial $B(z)$ [as in (34)] by solving the interpolation problem (42) with σ_n replaced by σ'_n .
- 2) Construct the Laurent polynomial

$$\Phi(z) = \sum_{k=-D+1}^{D-1} \Phi_k z^{-k} = 1 - \kappa B(z) \bar{B}(\bar{z}^{-1}). \quad (43)$$

- 3) Perform a polynomial spectral factorization of $\Phi(z)$. The result constitutes $A(z)$ [as in (34)].
- 4) Update $\sigma'_n \leftarrow \sigma_n \exp[j\angle A(z_n)]$.

Note that all steps can be implemented efficiently using the FFT [60, 8]. For the Steps 1 and 2, exploit the relation between discrete-time Fourier series and transform [60, 7.3]. Step 3 can be solved efficiently using $\mathcal{O}(OD \log(OD))$ flops, where O is an oversampling factor, using the Kolmogorov (or Hilbert transform) method for spectral factorization [61, B4]. We performed only three iterations in the numerical examples, in which case the total cost of this method remains $\mathcal{O}(OD \log(OD))$ flops.

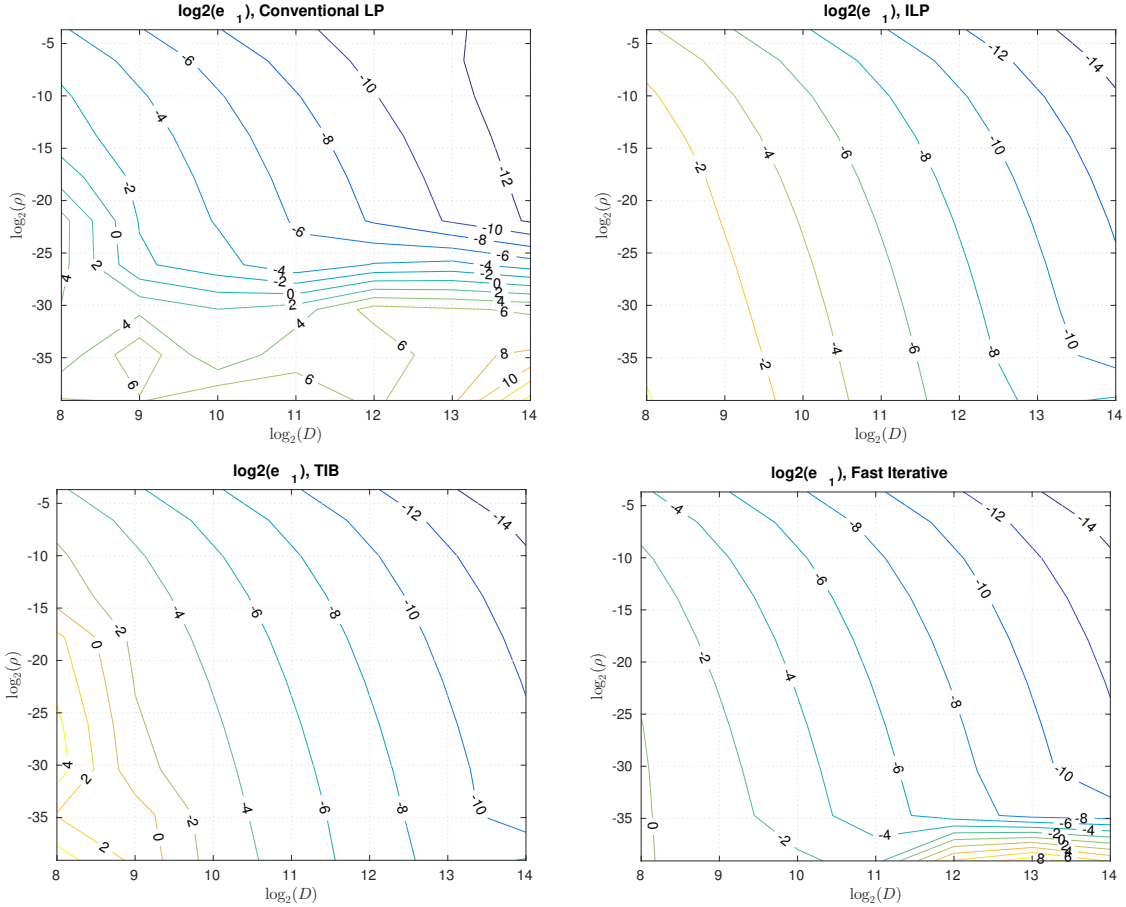


Figure 1. Simulation results for the hyperbolic secant with $T_2 = -T_1 = 2$.

C. Second Algorithm: Direct Synthesis

In our second algorithm, the synthesis step first generates $A(z)$ and then $B(z)$ through the following steps.

- 1) Find the polynomial $\phi(z) = \sum_{i=0}^{D-1} \phi_i z^{-i}$ that satisfies $\phi(z_n) = 1/\sqrt{1 + \kappa|\sigma_n|^2}$ [see (40)].
- 2) Construct the Laurent polynomial

$$\Phi(z) = \sum_{k=-D+1}^{D-1} \Phi_k z^{-k} = \phi(z)\bar{\phi}(\bar{z}^{-1}). \quad (44)$$

- 3) Perform a polynomial spectral factorization of $\Phi(z)$. The result constitutes $A(z)$ [as in (34)].
- 4) Construct $B(z)$ [as in (34)] by solving the interpolation problem $B(z_n) = A(z_n)\sigma_n$.

The computational complexity is again $\mathcal{O}(OD \log^2(OD))$ if the FFT is used. We do not iterate in this synthesis method.

D. Comparison of the Two Synthesis Methods

The advantage of our first iterative synthesis method is that the realizability conditions are, assuming infinite precision, met exactly after each iteration. We shall see later that this improves the numerical reliability of the overall inverse NFT. Its disadvantage is that it only works reliably for the defocusing case $\kappa = -1$. For $\kappa = +1$, the Laurent

polynomial (43) will in general no longer satisfy $\Phi(z) \geq 0$ for $|z| = 1$. This is a necessary condition for the spectral factorization, which then breaks down. The direct method avoids this problem since (44) satisfies $\Phi(z) \geq 0$ for $|z| = 1$ by construction. It is therefore also applicable if $\kappa = +1$. However, the realizability condition (35) is only guaranteed to be satisfied at the points $z = z_n$. It may not hold for other points $z \notin \{z_n\}$, leading to less numerical robustness.

Remark 6. Even though our second synthesis method enforces the realizability condition (35) only partially at the points $z = z_n$, we remark that it enforces the remaining conditions (36)–(37) fully, assuming exact arithmetic. Comparable synthesis methods in the literature, in contrast, do not enforce neither (35) nor (36) exactly [53], [28]. While enforcing (35) on a grid need not be an advantage per se (Runge’s phenomenon comes to mind), we will find later that our second synthesis method significantly outperforms a conventional benchmark method in a numerical example.

IV. NUMERICAL EXAMPLES

In this section, we compare our new fast algorithms with conventional ones in several numerical examples. We will not only investigate how the execution time and (yet to be defined) errors behave as the number of samples increases,

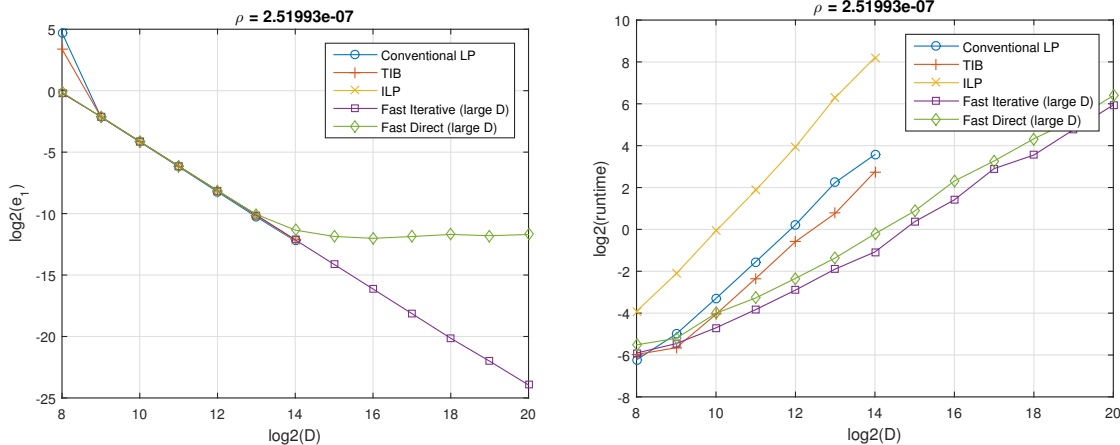


Figure 2. Errors and runtimes for the hyperbolic secant example with ρ fixed.

but also which influence scaling the provided continuous spectrum $\hat{q}(\lambda)$ up has on the error. In the context of fiber-optic communications, scaling the continuous spectrum up means increasing the energy of signal in the time-domain, and thus moving towards the highly nonlinear transmission regime. (This follows from nonlinear versions of Parseval's relation. See, e.g., [62, p. 4320]). The highly nonlinear regime is interesting for communication purposes because it offers increased signal-to-noise ratios, but it is also known to be numerically challenging for inverse NFT algorithms, especially in the defocusing case [49], [63]. The degree of nonlinearity will be expressed through the, to borrow a term from fiber Bragg grating design, *maximum reflectivity*

$$\rho = 1 - \max_{\lambda \in \mathbb{R}} |\hat{q}(\lambda)|, \quad \kappa = -1,$$

in the defocusing case, where one should note that $|\hat{q}(\lambda)| < 1$ in that case due to a continuous-time version of the realizability condition (35). (Dividing the latter by $|A(z)|^2$ shows that $|\hat{Q}(z)| \leq 1$.) In the focusing case, we instead use

$$\rho = 1 / \max_{\lambda \in \mathbb{R}} |\hat{q}(\lambda)|, \quad \kappa = +1,$$

to characterize the degree of nonlinearity. Note that smaller values of ρ imply increased nonlinearity in both cases.

A. Overview of the Algorithms

We will investigate the following algorithms.

1) *Fast Iterative Algorithm*: This is Algorithm 1 with the synthesis step from Section III-B. The oversampling factor used was $O = 8$. Three iterations were performed in each run. Among the three iterations, the wave functions that lead to the lowest mismatch in (38) in the squared sense was used.

2) *Fast Direct Algorithm*: This is Algorithm 1 with the synthesis step from Section III-C and $O = 8$.

3) *Conventional Layer Peeling (LP)*: This is the algorithm described by Skaar and Waagaard in [52, p. 1241]. They mention that a few iterations of steps 3 to 5 in their algorithm sometimes lead to improved results. In our results, iterating however could result in numerical instabilities and

we performed only the one run that is necessary. The FIR approximations in the Steps 4 and 7 were implemented using a FFT. The remaining operations were implemented using oversampled FFTs with an oversampling factor of eight. In the last step, layer peeling was used to generate the samples. The complexity of this algorithm is $\mathcal{O}(D^2)$.

4) *Toeplitz Bordering Method (TIB)*: This is the method to solve the GLM equations described in Belai et al. in [48]. The complexity of this algorithm is also $\mathcal{O}(D^2)$.

5) *Integral Layer Peeling (ILP)*: This the algorithm by Rosenthal and Horowitz from [49]. It was sped up using the Born approximation as described in [49, IV]. Each layer contained only one sample point for maximal accuracy, leading to an overall complexity of $\mathcal{O}(D^2 \log D)$.

B. Error Criteria

In order to assess the performance of the different algorithms, two different errors will be considered.

- 1) The first error compares the samples q'_n generated by the algorithm to known exact values q_n in (16),

$$e_1 = \left(\sum_{n=0}^{D-1} |q_n - q'_n|^2 \right) / \left(\sum_{n=0}^{D-1} |q_n|^2 \right). \quad (45)$$

Note that using midpoints $(t_n + t_{n+1})/2$ in (16) is essential for achieving a quadratic error [34, p. 175].

- 2) For the second error, the samples q'_n generated by the algorithm are used to generate a signal $q'(t)$ that is piecewise constant on the intervals. That is, $q'(t) = q_n$ for $t \in [t_n, t_{n+1})$. The continuous spectrum $\hat{q}'(\lambda)$ of this piecewise constant signal can be computed exactly (up to finite precision effects) using the T -matrix method [36], [37]. The difference between the continuous spectrum of the piecewise constant signal and the specified continuous spectrum is measured as

$$e_2 = \left(\sum_{n=0}^{D-1} |\hat{q}(\lambda_n) - \hat{q}'(\lambda_n)|^2 \right) / \left(\sum_{n=0}^{D-1} |\hat{q}_n(\lambda_n)|^2 \right), \quad (46)$$

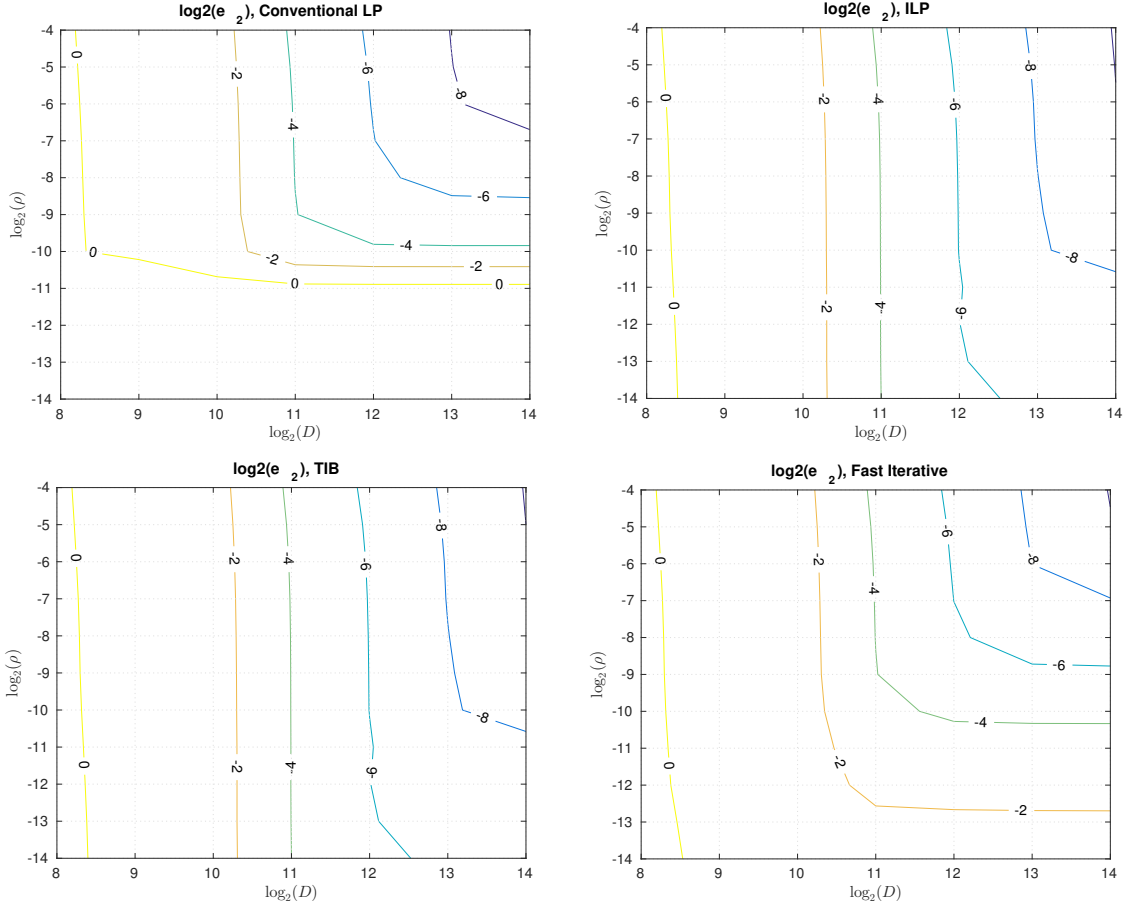


Figure 3. Simulation results for the eight raised cosines with $\kappa = -1$, $T_2 = -T_1 = 200$, $\lambda_{-1} = -5$ and $\lambda_D = 5$.

where $\lambda_n = \lambda_{-1} + (n + \frac{1}{2})\tilde{\delta}$ with $\tilde{\delta} = \frac{\lambda_D - \lambda_{-1}}{D}$. The constants λ_{-1} and λ_D will be specified per problem.

The error e_1 is simple to compute, but it can only be evaluated if the desired signal $q(t)$ is known analytically. Furthermore, it is not necessarily the error one is interested in practice because it is taken in the time domain. The error e_2 seems more relevant because it quantifies the difference between the specification and the continuous spectrum of a piecewise uniform signal realized using the output of the algorithm of interest. The disadvantage is that the terms $\hat{q}'(\lambda_n)$ in e_2 have to be computed numerically. Errors made while computing $\hat{q}'(\lambda_n)$ from the generated samples will turn up in e_2 even though they are not caused by the actual algorithm of interest. Furthermore, computing the $\hat{q}'(\lambda_n)$ requires $\mathcal{O}(D^2)$ flops, which can be significant.

C. First Example: Hyperbolic Secant, Defocusing Case

We first consider the example given in [48, Sec. 4]. The signal we try to recover is given by

$$q(t) = \frac{Q}{\mathcal{L}} \left(\operatorname{sech} \left(\frac{t}{\mathcal{L}} \right) \right)^{1-2i\mathcal{F}},$$

where \mathcal{F} , \mathcal{L} and Q are scalar parameters. We used $\mathcal{F} = 1.5$, $\mathcal{L} = \frac{1}{25}$, and varied Q from 0.5 to 5.5 in steps of 0.5. The

corresponding continuous spectrum is known to be

$$\hat{q}(\lambda) = -2^{-2i\mathcal{F}} Q \frac{\Gamma(d)\Gamma(f_-)\Gamma(f_+)}{\Gamma(\tilde{d})\Gamma(g_-)\Gamma(g_+)},$$

where $\Gamma(\cdot)$ is the gamma function, $d = \frac{1}{2} + i(\lambda\mathcal{L} - \mathcal{F})$, $f_{\pm} = \frac{1}{2} - i(\lambda\mathcal{L} \pm \sqrt{\mathcal{F}^2 + Q^2})$, and $g_{\pm} = 1 - i(\mathcal{F} \pm \sqrt{\mathcal{F}^2 + Q^2})$. The maximum reflectivity in this example is $\rho = 1 - |\hat{q}(0)|$.

The resulting error e_1 [see (45)] is shown in Figure 1 as a function of the maximum reflectivity ρ and the number of samples D for different algorithms. Our direct synthesis algorithm is not shown in this example because it performed very similar to conventional layer peeling. All algorithms perform worse as the maximum reflectivity increases, but our algorithm breaks down much later than conventional layer peeling. Integral layer peeling and Toeplitz inner bordering however did not break down for any of the considered values of Q , illustrating higher robustness at very high reflectivities.

A comparison of the error for a fixed ρ is shown in Figure 2 (left). Only the fast algorithms have been benchmarked for $D > 2^{14}$ samples because the conventional algorithms started to take very long. While all algorithms perform similar for $D \leq 2^{14}$, it is interesting to note that the direct method hits an error floor while the iterative method keeps improving. We attribute this to the fact that the direct algorithm does not ensure that the realizability conditions

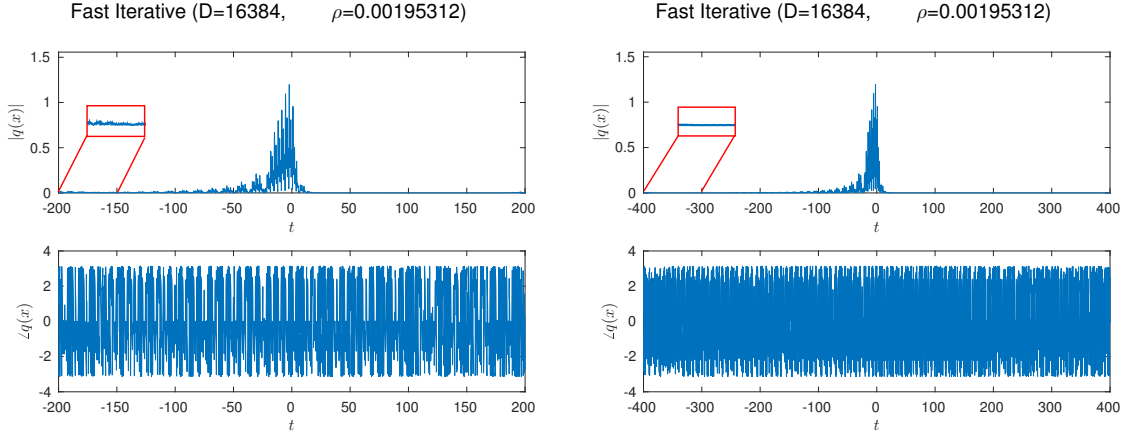


Figure 4. Grating profile generated by the fast iterative algorithm for the eight raised cosines with $\rho = 2^{-9}$ fixed, $\kappa = -1$, $\lambda_{-1} = -5$ and $\lambda_D = 5$. Left: With default value $T_2 = -T_1 = 200$. Right: $T_2 = -T_1 = 400$. The red boxes contain zoom-in's.

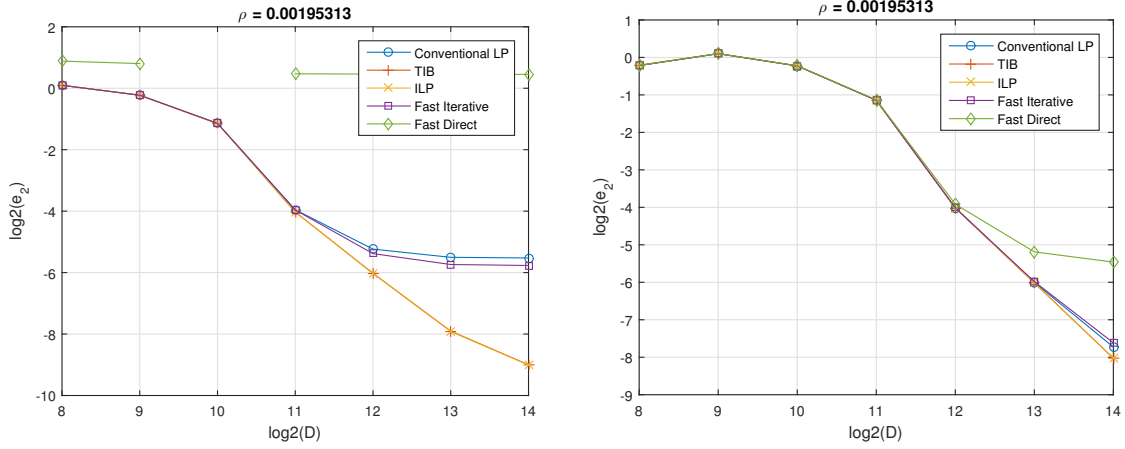


Figure 5. Errors for the raised cosines with $\rho = 2^{-9}$ fixed, $\kappa = -1$, $\lambda_{-1} = -5$ and $\lambda = 5$. Left: With $T_2 = -T_1 = 200$. Right: $T_2 = -T_1 = 400$.

(35)–(37) are met exactly, which leads to an error in the layer peeling step. The runtimes of the algorithms are shown in Figure 2 (right). Our fast methods achieve an almost linear increase in runtime as predicted, while the conventional algorithms exhibit quadratically growing runtimes.

D. Second Example: Eight Raised Cosines, Defocusing

This example is inspired by the numerical examples in [28] and [29]. The specified continuous spectrum is

$$\hat{q}(\lambda) = (1 - \rho) \sum_{k=0}^7 e^{i\phi_k} r(\lambda - c_k),$$

where the centers are $c_k = -3.5 + k$, the phases ϕ_k are randomly chosen from the set $\{\pm 0.25\pi, \pm 0.75\pi\}$, and

$$r(\lambda) = \begin{cases} 1, & |\lambda| \leq \frac{1-\beta}{2W} \\ \frac{1}{2} + \frac{1}{2} \cos\left(\frac{\pi W}{\beta} \left(|\lambda| - \frac{1-\beta}{2W}\right)\right), & \frac{1-\beta}{2W} < |\lambda| \leq \frac{1+\beta}{2W} \\ 0, & \text{otherwise} \end{cases}$$

is a normalized raised cosine filter with width $W = 2$ and roll-off factor $\beta = 0.5$. The maximal reflectivity is $\rho = 2^{-k}$, where $k = 1, \dots, 14$.

The resulting error e_2 [see (46)] is shown in Figure 3, again for different number of samples D and maximum reflectivities ρ . The observations are the same as in the previous example. Our fast iterative algorithm is more robust than conventional layer peeling, but less robust than integral layer peeling and Toeplitz inner bordering. We however note that the robustness of our algorithms (and conventional layer peeling) can be improved. Figure 4 (left) shows a typical case close to a breakdown, which is heralded through “artificial tails” in the generated grating profile. (Similar observations have been made in [29, Fig. 1].) We suspect that this phenomenon is a manifestation of a truncation error in the time domain, i.e., the signal $q(t)$ specified through the reflection coefficient $\hat{q}(\lambda)$ is non-zero for locations outside the interval $[T_1, T_2]$ that is considered by the inverse nonlinear Fourier transform algorithm. By doubling T_2 , we could get rid of the artificial ripple, as is shown in Figure 4 (right). Figure 5 shows the error e_2 for both values of $T_2 = -T_1$. The plots confirm that doubling T_2 improves the numerical accuracy of our fast iterative method such that it is very close to integral layer peeling and Toeplitz inner bordering. Note that the final error of the latter methods

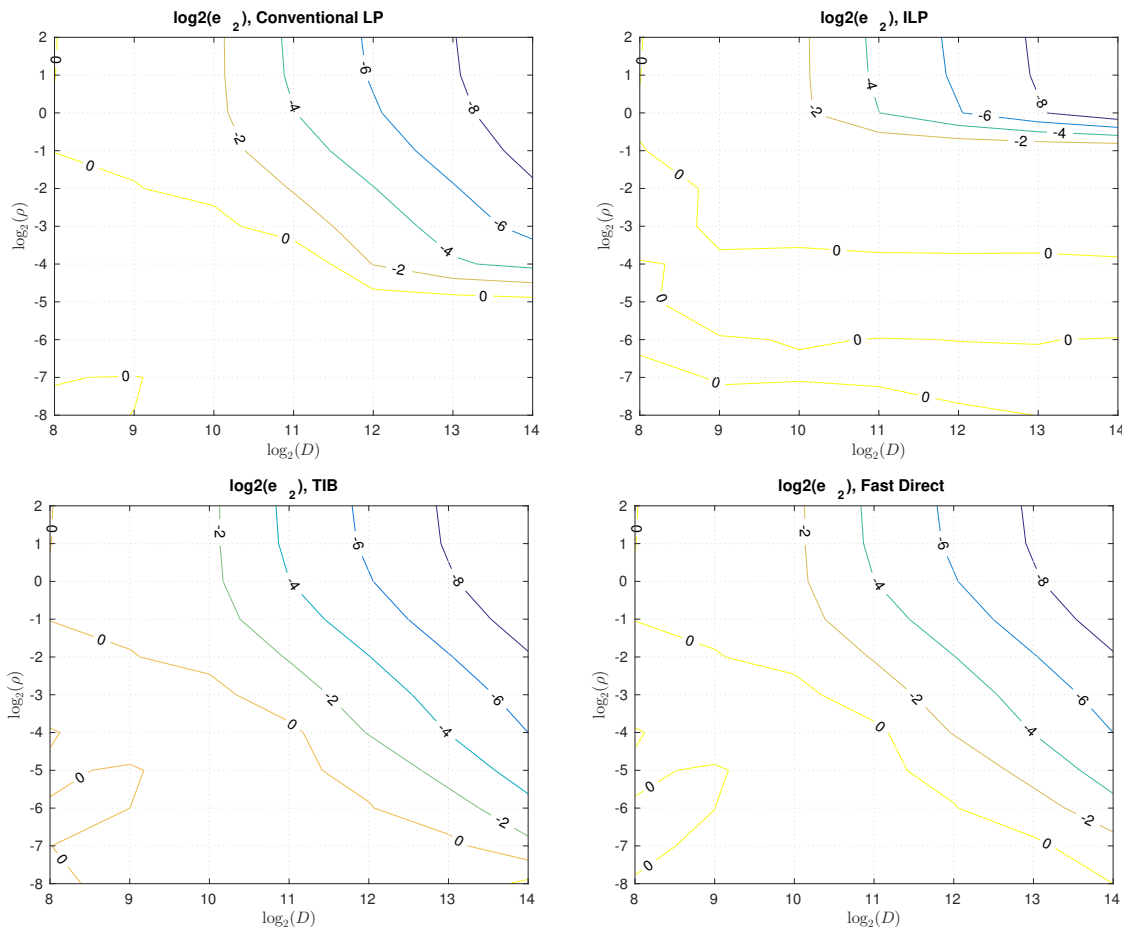


Figure 6. Simulation results for the eight raised cosines with $\kappa = +1$, $\lambda_{-1} = -5$ and $\lambda_D = 5$.

however slightly increases when T_2 is doubled. We attribute this to the reduced resolution ε in the spatial domain which could be brought back to its original value by doubling the number of samples D . We remark that for our fast algorithms, this would only double the computational costs, while it would quadruple it for the conventional algorithms.

E. Third Example: Eight Raised Cosines, Focusing

In our last example, we consider a positive sign κ in the Zakharov-Shabat problem, which corresponds to the focusing NSE. The continuous spectrum was

$$\hat{q}(\lambda) = \frac{1}{\rho} \sum_{k=0}^{\tau} e^{i\phi_k} r(\lambda - c_k),$$

where all values are as in the previous example except that $\rho = 2^k$ for $k = 2, 1, \dots, -8$. [Note that while continuous spectrum cannot have absolute values larger than one if κ is negative due to (35), this is well possible if κ is positive.] The algorithms were adapted by simply changing signs were necessary. The resulting errors are shown in Figure 6. The errors of all algorithms increase with the maximum absolute value ρ^{-1} of the continuous spectrum, but surprisingly this time integral layer peeling breaks down first. We do not

have a good explanation for this phenomenon at the moment. Conventional layer peeling also breaks down early, while no breakdown can be observed for Toeplitz inner bordering and our fast direct method. Both methods perform equally well. Our fast iterative method breaks down before conventional layer peeling and is therefore not shown.

V. CONCLUSION

In this paper, two new fast inverse nonlinear Fourier transform algorithms for nonlinear Fourier spectra with empty discrete part have been proposed and evaluated in numerical experiments. Both algorithms require only $\mathcal{O}(D \log^2 D)$ flops, D being the number of samples, which is almost an order of magnitude faster than conventional algorithms. The first proposed algorithm is iterative and excels in the defocusing case (i.e., if the sign κ in the nonlinear Schrödinger equation is negative), in which case it is both faster and more robust than conventional layer peeling. Although our first algorithm still broke down earlier than integral layer peeling and Toeplitz inner bordering, both of which are based on discretizing the GLM equations, it also turned out that the breakdown could be avoided by increasing the time window. A detailed investigation of this issue and associated trade-offs is left for future research. The second proposed

algorithm is direct and excels in the focusing case (i.e., for positive κ). In our example it performed as good as the best conventional algorithm while being significantly faster.

APPENDIX: PROOF OF THEOREM 1

In this appendix, Theorem 1 is proven. The proof rests on several auxiliary results that need to be introduced first.

A. The Normalized Zakharov-Shabat System

In this subsection, the Zakharov-Shabat system (1) is transformed such that certain bounds can be derived more easily. For the choice $[T_1, T_2] = [T_0 - m\delta, T_0 + m\delta]$ in Theorem 1, the initial condition (9) becomes

$$e^{j\lambda T_1} \phi(T_1, \lambda) = e^{j\lambda(T_0 - m\delta)} \phi(T_0 - m\delta, \lambda) = \begin{bmatrix} 1 \\ 0 \end{bmatrix}. \quad (47)$$

Let us denote the solution of the Zakharov-Shabat system that satisfies the initial condition (47) for a specific choice of $m = 1, 2, \dots$ by $\phi^m(t, \lambda)$. We introduce the matrices

$$\mathbf{E}(t, \lambda) := \begin{bmatrix} j\lambda & q(t) \\ -\kappa\bar{q}(t) & -j\lambda \end{bmatrix}, \quad \mathbf{F}(t, \lambda) := \begin{bmatrix} e^{j\lambda t} & 0 \\ 0 & e^{-j\lambda t} \end{bmatrix}.$$

The Zakharov-Shabat system can now be written as

$$\frac{d\phi^m}{dt} = \mathbf{E}\phi^m, \quad [\mathbf{F}\phi^m](T_0 - m\delta, \lambda) = \begin{bmatrix} 1 \\ 0 \end{bmatrix}. \quad (48)$$

In the following, it will be convenient to work with the normalized wave functions

$$\varphi^m(t, \lambda) = \begin{bmatrix} \varphi_1^m(t, \lambda) \\ \varphi_2^m(t, \lambda) \end{bmatrix} := \mathbf{F}(t, \lambda)\phi^m(t, \lambda). \quad (49)$$

Replacing ϕ^m in (48) with φ^m leads to $\frac{d}{dt}(\mathbf{F}^{-1}\varphi^m) = \mathbf{E}\mathbf{F}^{-1}\varphi^m$. Solving for $\frac{d}{dt}\varphi^m$ leads to a normalized version of the Zakharov-Shabat system with initial condition (47),

$$\frac{d\varphi^m}{dt} = \mathbf{A}\varphi^m, \quad (50)$$

$$\varphi^m(T_0 - m\delta, \lambda) = \begin{bmatrix} 1 \\ 0 \end{bmatrix}, \quad (51)$$

where the state matrix $\mathbf{A} := \mathbf{F}^{-1}(\mathbf{E}\mathbf{F} - \frac{d\mathbf{F}}{dt})$ satisfies

$$\mathbf{A}(t, \lambda) = \begin{bmatrix} 0 & q(t)e^{-2j\lambda t} \\ -\kappa e^{2j\lambda t}\bar{q}(t) & 0 \end{bmatrix}. \quad (52)$$

Remember that, due to the definition of the NFT (5)–(7), only values of λ with $\Im\lambda \geq 0$ are of interest. One of the exponentials in the state matrix (52) increases exponentially for $\Im\lambda > 0$, but, on the other hand, the signal $q(t)$ was assumed to decay exponentially fast in (1). The first effect is in general outweighed by the second only if

$$0 \leq \Im\lambda \leq d_0 < d, \quad (53)$$

which is an assumption made in Theorem 1.

B. Transition Matrices

The normalized Zakharov-Shabat system (50) is linear. Therefore, for any finite t_0, t_1 with $t_0 \leq t_1$, there exists a unique *transition matrix* $\Phi(t_1, t_0; \lambda)$ such that [64, p. 8]

$$\varphi(t_1, \lambda) = \Phi(t_1, t_0; \lambda)\varphi(t_0, \lambda) \quad (54)$$

for *any* solution φ . The transition matrix is given by the Peano-Baker series [64, Lem. 1.7.2]

$$\begin{aligned} \Phi(t_1, t_0; \lambda) &= \mathbf{I} + \int_{t_0}^{t_1} \mathbf{A}(\sigma_1, \lambda) d\sigma_1 \\ &+ \int_{t_0}^{t_1} \mathbf{A}(\sigma_1, \lambda) \int_{t_0}^{\sigma_1} \mathbf{A}(\sigma_2, \lambda) d\sigma_2 d\sigma_1 \\ &+ \int_{t_0}^{t_1} \mathbf{A}(\sigma_1, \lambda) \int_{t_0}^{\sigma_1} \mathbf{A}(\sigma_2, \lambda) \int_{t_0}^{\sigma_2} \mathbf{A}(\sigma_3, \lambda) d\sigma_3 d\sigma_2 d\sigma_1 \\ &+ \dots \end{aligned} \quad (55)$$

To simplify notation, we now introduce the two grids

$$s_m^\pm := T_0 \pm m\delta, \quad m = 0, 1, 2, \dots \quad (56)$$

Their ordering is illustrated below,

$$\dots < s_2^- < s_1^- < s_0^- = T_0 = s_0^+ < s_1^+ < s_2^+ < \dots$$

With the notation established so far, the approximations of $\alpha(\lambda)$ and $\beta(\lambda)$ introduced in Theorem 1 can be written as

$$\begin{aligned} \begin{bmatrix} \tilde{\alpha}^m(\lambda) \\ \tilde{\beta}^m(\lambda) \end{bmatrix} &\stackrel{(49)}{=} \varphi^m(s_m^+, \lambda) \\ &\stackrel{(54)}{=} \Phi(s_m^+, s_m^-; \lambda)\varphi^m(s_m^-, \lambda) \\ &\stackrel{(47)}{=} \Phi(s_m^+, s_m^-; \lambda) \begin{bmatrix} 1 \\ 0 \end{bmatrix}. \end{aligned} \quad (57)$$

The sequence $\Phi(s_m^+, s_m^-; \lambda)$ is seen to play a fundamental role from this formula. It will therefore be analyzed next.

C. Analysis of the Sequence $\Phi(s_m^+, s_m^-; \lambda)$

For any m , we define the transition matrices

$$\Phi_m^+(\lambda) := \Phi(s_m^+, s_{m-1}^+; \lambda), \quad (58)$$

$$\Phi_m^-(\lambda) := \Phi(s_{m-1}^-, s_m^-; \lambda). \quad (59)$$

They will be essential during for the analysis of the sequence $\Phi(s_m^+, s_m^-; \lambda)$. The next lemma quantifies their decay.

Lemma 7. *Let λ satisfy the condition (53), and let $m_0 = m_0(T_0, \delta)$ denote the smallest m such that zero is contained in the open interval (s_m^-, s_m^+) ,*

$$m_0 := \min \left\{ m = 1, 2, \dots : s_m^- < 0 < s_m^+ \right\}. \quad (60)$$

Furthermore, introduce the constants

$$\mu := e^{-2(d-d_0)\delta} \in (0, 1), \quad C_1 := c\mu^{-m_0} \in (0, \infty),$$

where c and d are given in (1) and T_0 and δ are given in Theorem 1. Then, for all $m = 1, 2, \dots$,

$$\|\Phi_m^\pm(\lambda)\| \leq 1 + \frac{C_1}{1-\mu}\mu^m, \quad \|\Phi_m^\pm(\lambda) - \mathbf{I}\| \leq \frac{C_1}{1-\mu}\mu^m,$$

where $\|\cdot\| := \sup_{\|x\|=1} \|\cdot x\|$ denotes the spectral norm.

Remark 8. The constants μ and C_1 in this lemma depend on c, d, δ, T_0 as well as d_0 , but not on λ or m .

Proof: The norm of the state matrix (52) satisfies

$$\begin{aligned} \|\mathbf{A}(t, \lambda)\| &= \max_{\sigma \in \{\pm 1\}} |q(t)| |e^{2\sigma j \lambda t}| \stackrel{(53)}{=} |q(t)| e^{2\Im \lambda |t|} \\ &\stackrel{(1)}{\leq} c e^{-2(d-\Im \lambda)|t|} \stackrel{(53)}{\leq} c e^{-2(d-d_0)|t|}, \end{aligned} \quad (61)$$

Whenever $m > m_0$,

$$\begin{aligned} &\sup_{s \in [s_m^-, s_{m-1}^-]} \|\mathbf{A}(s, \lambda)\| \\ &\stackrel{(61)}{\leq} c \sup_{s \in [s_m^-, s_{m-1}^-]} e^{-2(d-d_0)|s_{m-1}^- + s|} \\ &\left(\begin{array}{l} s_m^- < s_{m-1}^- < 0 \\ \text{if } m > m_0 \end{array} \right) \stackrel{(56)}{=} c e^{-2(d-d_0)|s_{m-1}^-|} \\ &\leq c e^{-2(d-d_0)(|T_0| + (m-1)\delta)} \\ &= c \underbrace{e^{-2(d-d_0)|T_0|}}_{\leq 1} \underbrace{e^{2(d-d_0)\delta}}_{=\mu^{-1}} \underbrace{e^{-2(d-d_0)m\delta}}_{=\mu^m} \\ &\leq C_1 \mu^m. \end{aligned} \quad (62)$$

On the other hand, whenever $m \leq m_0$,

$$\begin{aligned} \sup_{s \in [s_m^-, s_{m-1}^-]} \|\mathbf{A}(s, \lambda)\| &\leq c \sup_{s \in [s_m^-, s_{m-1}^-]} \underbrace{e^{-2(d-d_0)|s|}}_{\leq 1} \\ &\leq c \underbrace{\mu^{-m_0} \mu^m}_{\geq 1} = C_1 \mu^m. \end{aligned} \quad (63)$$

Combining (62) and (63), we find that

$$\sup_{s \in [s_m^-, s_{m-1}^-]} \|\mathbf{A}(s, \lambda)\| \leq C_1 \mu^m, \quad \text{for any } m.$$

The Peano-Baker series (55) now implies

$$\begin{aligned} \|\Phi_m^-(\lambda)\| &\leq 1 + C_1 [(\mu^m)^1 + (\mu^m)^2 + \dots] \\ &= 1 + \frac{C_1 \mu^m}{1 - \mu^m} \leq 1 + \frac{C_1}{1 - \mu} \mu^m, \\ \|\Phi(s_m^-, s_{m-1}^-; \lambda) - \mathbf{I}\| &\leq C_1 [(\mu^m)^1 + (\mu^m)^2 + \dots] \\ &= \frac{C_1 \mu^m}{1 - \mu^m} \leq \frac{C_1}{1 - \mu} \mu^m. \end{aligned}$$

The other two claimed inequalities can be shown in the the same way. The derivations are thus omitted. \blacksquare

The next lemma establishes the boundedness of the aforementioned sequence of transition matrices, $\Phi(s_m^+, s_m^-; \lambda)$.

Lemma 9. For any λ as in (53), we have

$$\sup_{m=1,2,\dots} \|\Phi(s_m^+, s_m^-; \lambda)\| \leq C_2,$$

where $C_2 := \exp\left(\frac{2C_1\mu}{(1-\mu)^2}\right)$ with μ and C_1 as in Lemma 7.

Proof: The transition matrix can be written as

$$\Phi(s_m^+, s_m^-; \lambda) = \Phi_m^+(\lambda) \Phi(s_{m-1}^+, s_{m-1}^-; \lambda) \Phi_m^-(\lambda) \quad (64)$$

for Φ_m^\pm as in (58)–(59). Using this result, we find that

$$\begin{aligned} \|\Phi(s_m^+, s_m^-; \lambda)\| &\stackrel{(64)}{\leq} \|\Phi_m^+(\lambda)\| \|\Phi(s_{m-1}^+, s_{m-1}^-; \lambda)\| \\ &\quad \times \|\Phi_m^-(\lambda)\| \\ &\text{(iterate)} \stackrel{(\dots)}{\leq} \left(\prod_{l=1}^m \|\Phi_l^+(\lambda)\| \right) \underbrace{\|\Phi(s_0^+, s_0^-; \lambda)\|}_{=\|\mathbf{I}\|=1} \\ &\quad \times \left(\prod_{l=1}^m \|\Phi_l^-(\lambda)\| \right) \\ &\text{(Lemma 7)} \leq \prod_{l=1}^m \left(1 + \frac{C_1}{1 - \mu} \mu^m \right)^2 \\ &\left(\begin{array}{l} ab = e^{\ln a + \ln b} \\ \ln a^2 = 2 \ln a \end{array} \right) = \exp \left(2 \sum_{l=1}^m \ln \left(1 + \frac{C_1}{1 - \mu} \mu^m \right) \right) \\ &\left(\begin{array}{l} \ln(1+x) \leq x \\ \text{for } x \geq 0 \end{array} \right) \leq \exp \left(\frac{2C_1}{1 - \mu} \sum_{l=1}^m \mu^m \right) \\ &\leq \exp \left(\frac{2C_1}{1 - \mu} \frac{\mu}{1 - \mu} \right) = C_2. \end{aligned}$$

The next lemma finally establishes the convergence of the sequence of transition matrices of interest.

Lemma 10. The limit $\Phi^\infty(\lambda) := \lim_{m \rightarrow \infty} \Phi(s_m^+, s_m^-; \lambda)$ is well-defined for any λ as in (53). For any $m \in \{1, 2, \dots\}$,

$$\|\Phi^\infty(\lambda) - \Phi(s_m^+, s_m^-; \lambda)\| \leq C_3 \mu^m,$$

where, with μ and C_1 as in Lem. 7, and C_2 as in Lem. 9,

$$C_3 := C_1 C_2 \frac{\mu}{(1 - \mu)^2} \left[2 + \frac{C_1}{1 - \mu} \right].$$

Proof: Using Lemma 7, we find that

$$\begin{aligned} &\|\Phi(s_m^+, s_m^-; \lambda) - \Phi(s_{m-1}^+, s_{m-1}^-; \lambda)\| \\ &\stackrel{(64)}{=} \|\Phi_m^+(\lambda) \Phi(s_{m-1}^+, s_{m-1}^-; \lambda) \Phi_m^-(\lambda) - \Phi(s_{m-1}^+, s_{m-1}^-; \lambda) \\ &\quad + \underbrace{\Phi(s_{m-1}^+, s_{m-1}^-; \lambda) \Phi_m^-(\lambda) - \Phi(s_{m-1}^+, s_{m-1}^-; \lambda) \Phi_m^-(\lambda)}_{=0}\| \\ &\leq \|[\Phi_m^+(\lambda) - \mathbf{I}] \Phi(s_{m-1}^+, s_{m-1}^-; \lambda) \Phi_m^-(\lambda)\| \\ &\quad + \|\Phi(s_{m-1}^+, s_{m-1}^-; \lambda) [\Phi_m^-(\lambda) - \mathbf{I}]\| \\ &\leq \|\Phi(s_{m-1}^+, s_{m-1}^-; \lambda)\| (\|\Phi_m^+(\lambda) - \mathbf{I}\| \|\Phi_m^-(\lambda)\| \\ &\quad + \|\Phi_m^-(\lambda) - \mathbf{I}\|) \\ &\leq C_2 \left[\frac{C_1}{1 - \mu} \mu^m \left(1 + \frac{C_1}{1 - \mu} \mu^m \right) + \frac{C_1}{1 - \mu} \mu^m \right] \\ &= \frac{C_1 C_2}{1 - \mu} \left(2 + \frac{C_1}{1 - \mu} \mu^m \right) \mu^m \\ &\leq \frac{C_1 C_2}{1 - \mu} \left(2 + \frac{C_1}{1 - \mu} \right) \mu^m. \end{aligned} \quad (65)$$

The limit can be written as

$$\begin{aligned} \Phi^\infty(\lambda) &= \Phi(s_m^+, s_m^-; \lambda) \\ &+ \sum_{l=m+1}^{\infty} [\Phi(s_l^+, s_l^-; \lambda) - \Phi(s_{l-1}^+, s_{l-1}^-; \lambda)]. \end{aligned} \quad (66)$$

The infinite series in this representation converges since

$$\begin{aligned} & \sum_{l=m+1}^{\infty} \|\Phi(s_l^+, s_l^-; \lambda) - \Phi(s_{l-1}^+, s_{l-1}^-; \lambda)\| \\ & \stackrel{(65)}{\leq} \frac{C_1 C_2}{1-\mu} \left(2 + \frac{C_1}{1-\mu}\right) \sum_{l=m+1}^{\infty} \mu^l = C_3 \mu^m. \end{aligned} \quad (67)$$

which implies that the limit is well-defined. Rearranging the terms in (66) finally proves the second claim,

$$\begin{aligned} & \|\Phi^\infty(\lambda) - \Phi(s_m^+, s_m^-; \lambda)\| \\ & \leq \sum_{l=m+1}^{\infty} \|\Phi(s_l^+, s_l^-; \lambda) - \Phi(s_{l-1}^+, s_{l-1}^-; \lambda)\| \stackrel{(67)}{=} C_3 \mu^m. \end{aligned}$$

D. The Limiting Function φ^∞

The auxiliary results derived so far are sufficient to show that the estimates $\tilde{\alpha}^m(\lambda)$ and $\tilde{\beta}^m(\lambda)$ converge, but they are not sufficient to show that their limit is $\alpha(\lambda)$ and $\beta(\lambda)$, respectively. In this subsection, we analyze the function

$$\varphi^\infty(t, \lambda) := \lim_{m \rightarrow \infty} \varphi^m(t, \lambda), \quad t \in \mathbb{R}, \quad (68)$$

in order to deliver the arguments for this last step.

Lemma 11. *Fix any λ as in (53). Then, $\varphi^\infty(t, \lambda)$ in (68) is well-defined for any $t \in \mathbb{R}$, i.e., the limit exists and is finite. Furthermore, for any t_0 there exists a $\delta = \delta(t_0) > 0$ such that the sequence $\varphi^m(t, \lambda)$, $m = 1, 2, \dots$, converges uniformly towards $\varphi^\infty(t, \lambda)$ on the interval $[t_0 - \delta, t_0 + \delta]$.*

Proof: Fix any t_0 , and let the smallest $m \in \{1, 2, \dots\}$ such that $s_m^- < t_0$ be $m_1 = m_1(t_0)$. The sequence

$$\mathbf{X}_{m_1}^m := \Phi_{m_1+1}^- \Phi_{m_1+2}^- \times \dots \times \Phi_m^-, \quad m > m_1,$$

converges with a finite limit $\mathbf{X}_{m_1}^\infty$ by Lemma 7. (A similar argument as in the proof of Lemma 9 applies.) Hence,

$$\begin{aligned} \varphi^\infty(t, \lambda) &= \lim_{m \rightarrow \infty} \underbrace{\Phi(t, s_{m_1}^-) \mathbf{X}_{m_1}^m}_{=\Phi(t, s_m^-)} \begin{bmatrix} 1 \\ 0 \end{bmatrix} \\ &= \Phi(t, s_{m_1}^-) \mathbf{X}_{m_1}^\infty \begin{bmatrix} 1 \\ 0 \end{bmatrix}, \quad \forall t \geq s_{m_1}^-, \end{aligned} \quad (69)$$

which implies that the limit $\varphi^\infty(t, \lambda)$ exists and is finite for any t . The transition matrix $\Phi(t, s_{m_1}^-)$ is a continuous function of t . (Both columns of $\Phi(t, s_{m_1}^-)$ are solutions of (50) for the appropriate initial conditions. As such, they are absolutely continuous. See [64, Def. 1.2.1+p. 8].) Hence,

$$S := \sup_{t \in [t_0 - \delta, t_0 + \delta]} \|\Phi(t, s_{m_1}^-)\| < \infty,$$

where $\delta = \delta(t_0) > 0$ is an arbitrary constant small enough such that $s_{m_1}^- < t_0 - \delta$. As the term $\mathbf{X}_{m_1}^\infty$ in (69) is independent of t , the sequence $\varphi^m(t, \lambda)$ is finally found to converge uniformly to $\varphi^\infty(t, \lambda)$ on the interval $[t_0 - \delta, t_0 + \delta]$:

$$\begin{aligned} & \|\varphi^\infty(t, \lambda) - \varphi^m(t, \lambda)\| \\ &= \left\| \Phi(t, s_{m_1}^-) [\mathbf{X}_{m_1}^\infty - \mathbf{X}_{m_1}^m] \begin{bmatrix} 1 \\ 0 \end{bmatrix} \right\| \leq S \|\mathbf{X}_{m_1}^\infty - \mathbf{X}_{m_1}^m\|. \end{aligned}$$

With the well-definedness of φ^∞ being established, φ^∞ is now shown to solve the normalized Zakarov-Shabat system. ■

Lemma 12. *Fix any λ as in (53). Then, $\varphi^\infty(t, \lambda)$ given in (68) solves the normalized Zakarov-Shabat system (50).*

Proof: Fix any t_0 and choose, in light of Lemma 11, $\delta = \delta(t_0) > 0$ such that $\varphi^m(t, \lambda)$ converges uniformly towards $\varphi^\infty(t, \lambda)$ on $[t_0 - \delta, t_0 + \delta]$. Then, the sequence

$$\frac{d\varphi^m}{dt}(t, \lambda) \stackrel{(50)}{=} \mathbf{A}(t, \lambda) \varphi^m(t, \lambda)$$

also converges on $[t_0 - \delta, t_0 + \delta]$, with limit

$$\mathbf{g}(t, \lambda) := \lim_{m \rightarrow \infty} \frac{d\varphi^m}{dt}(t, \lambda) = \mathbf{A}(t, \lambda) \varphi^\infty(t, \lambda). \quad (70)$$

The convergence is again uniform because

$$\begin{aligned} \left\| \mathbf{g}(t, \lambda) - \frac{d\varphi^m}{dt}(t, \lambda) \right\| &= \|\mathbf{A}(t, \lambda) [\varphi^\infty(t, \lambda) - \varphi^m(t, \lambda)]\| \\ &\leq \underbrace{\|\mathbf{A}(t, \lambda)\|}_{\leq c \text{ via (61)}} \|\varphi^\infty(t, \lambda) - \varphi^m(t, \lambda)\|. \end{aligned}$$

Theorem 7.17 in [65] now shows that

$$\frac{d\varphi^\infty}{dt}(t_0, \lambda) = \mathbf{g}(t_0, \lambda). \quad (71)$$

Combining (70) and (71) leads to

$$\frac{d\varphi^\infty}{dt}(t_0, \lambda) = \mathbf{A}(t_0, \lambda) \varphi^\infty(t_0, \lambda).$$

Since t_0 can be chosen arbitrarily, the lemma is proven. ■

Finally, the initial condition fulfilled by φ^∞ is determined.

Lemma 13. *Fix any λ as in (53). Then, $\varphi^\infty(t, \lambda)$ given in (68) converges for $t \rightarrow -\infty$ with limit*

$$\lim_{t \rightarrow -\infty} \varphi^\infty(t, \lambda) = \begin{bmatrix} 1 \\ 0 \end{bmatrix}. \quad (72)$$

Proof: Recall the representation (69), where $m_1 = m_1(t_0)$. The first term in this presentation satisfies

$$\lim_{t_0 \rightarrow -\infty} \Phi(t_0, s_{m_1(t_0)}^-) \stackrel{(55),(61)}{=} \mathbf{I}.$$

On the other hand, the second term satisfies

$$\lim_{t_0 \rightarrow -\infty} \mathbf{X}_{m_1(t_0)}^\infty \stackrel{(\text{Lem. 7})}{=} \mathbf{I}.$$

Hence, as claimed,

$$\lim_{t_0 \rightarrow -\infty} \varphi^\infty(t_0, \lambda) \stackrel{(69)}{=} (\mathbf{I} \times \mathbf{I}) \begin{bmatrix} 1 \\ 0 \end{bmatrix} = \begin{bmatrix} 1 \\ 0 \end{bmatrix}. \quad \blacksquare$$

E. Proof of Theorem 1

We are finally ready to prove Theorem 1.

Proof: Lemma 10 shows that the limit

$$\begin{bmatrix} \tilde{\alpha}^\infty(\lambda) \\ \tilde{\beta}^\infty(\lambda) \end{bmatrix} := \lim_{m \rightarrow \infty} \begin{bmatrix} \tilde{\alpha}^m(\lambda) \\ \tilde{\beta}^m(\lambda) \end{bmatrix} \stackrel{(57)}{=} \Phi^\infty(\lambda) \begin{bmatrix} 1 \\ 0 \end{bmatrix},$$

exists and is finite, with

$$\begin{aligned} & \left\| \begin{bmatrix} \tilde{\alpha}^\infty(\lambda) \\ \tilde{\beta}^\infty(\lambda) \end{bmatrix} - \begin{bmatrix} \tilde{\alpha}^m(\lambda) \\ \tilde{\beta}^m(\lambda) \end{bmatrix} \right\| \\ & \stackrel{(57)}{\leq} \|\Phi^\infty(\lambda) - \Phi(s_m^+, s_m^-; \lambda)\| \leq C_3 \mu^m. \end{aligned}$$

It remains to show that $\tilde{\alpha}^\infty(\lambda) = \alpha(\lambda)$ and $\tilde{\beta}^\infty(\lambda) = \beta(\lambda)$, respectively. The Lemmas 12 and 13 show that φ^∞ solves the normalized Zakharov-Shabat system (50) with boundary condition (72). By [64, Th. 1.2.1], it is the only such solution. Theorem 1.5.2 in [64] ensures that the limit

$$\varphi^\infty(\infty, \lambda) := \lim_{t \rightarrow +\infty} \varphi^\infty(t, \lambda) \stackrel{(49)}{=} \begin{bmatrix} \alpha(\lambda) \\ \beta(\lambda) \end{bmatrix}$$

exists and is finite. Thus,

$$\lim_{m \rightarrow \infty} \|\varphi^\infty(\infty, \lambda) - \varphi^\infty(s_m^+, \lambda)\| = 0. \quad (73)$$

On the other hand, in light of the Lemmas 10 and 13,

$$\begin{aligned} & \lim_{m \rightarrow \infty} \|\varphi^\infty(s_m^+, \lambda) - \varphi^m(s_m^+, \lambda)\| \\ & \stackrel{(54)}{=} \lim_{m \rightarrow \infty} \|\Phi(s_m^+, s_m^-; \lambda) (\varphi^\infty(s_m^-, \lambda) - \varphi^m(s_m^-, \lambda))\| \\ & \stackrel{(51)}{=} \lim_{m \rightarrow \infty} \left\| \Phi(s_m^+, s_m^-; \lambda) \left(\varphi^\infty(s_m^-, \lambda) - \begin{bmatrix} 1 \\ 0 \end{bmatrix} \right) \right\| \\ & = \left\| \Phi^\infty(\lambda) \left(\begin{bmatrix} 1 \\ 0 \end{bmatrix} - \begin{bmatrix} 1 \\ 0 \end{bmatrix} \right) \right\| = 0. \end{aligned} \quad (74)$$

Combining these two results finally shows that

$$\begin{aligned} & \left\| \begin{bmatrix} \alpha(\lambda) \\ \beta(\lambda) \end{bmatrix} - \begin{bmatrix} \tilde{\alpha}^m(\lambda) \\ \tilde{\beta}^m(\lambda) \end{bmatrix} \right\| \\ & = \|\varphi^\infty(\infty, \lambda) - \varphi^m(s_m^+, \lambda)\| \\ & \quad + \underbrace{\|\varphi^\infty(s_m^+, \lambda) - \varphi^m(s_m^+, \lambda)\|}_{=0} \\ & \leq \|\varphi^\infty(\infty, \lambda) - \varphi^\infty(s_m^+, \lambda)\| \\ & \quad + \|\varphi^\infty(s_m^+, \lambda) - \varphi^m(s_m^+, \lambda)\| \xrightarrow[(73),(74)]{m \rightarrow \infty} 0. \end{aligned}$$

Thus, $\tilde{\alpha}^\infty(\lambda) = \alpha(\lambda)$ and $\tilde{\beta}^\infty(\lambda) = \beta(\lambda)$ as claimed. ■

REFERENCES

- [1] V. F. Zakharov and A. B. Shabat, "Exact theory of two-dimensional self-focusing and one-dimensional self-modulation of waves in nonlinear media," *Sov. Phys. JETP*, vol. 34, pp. 62–69, Jan. 1972.
- [2] J. Skaar, L. Wang, and T. Erdogan, "On the synthesis of fiber Bragg gratings by layer peeling," *IEEE J. Quant. Electron.*, vol. 37, no. 2, pp. 165–173, 2001.
- [3] D. E. Rourke and P. G. Morris, "The inverse scattering transform and its use in the exact inversion of the Bloch equation for noninteracting spins," *J. Magn. Reson.*, vol. 99, pp. 118–138, 1992.
- [4] C. L. Epstein, "Minimum energy pulse synthesis via the inverse scattering transform," *J. Magn. Reson.*, vol. 167, pp. 185–210, 2004.
- [5] H. B. Thacker, "Exact integrability in quantum field theory and statistical systems," *Rev. Mod. Phys.*, vol. 53, no. 2, pp. 253–286, 1981.
- [6] A. M. Bruckstein, B. C. Levy, and T. Kailath, "Differential methods in inverse scattering," *SIAM J. Appl. Math.*, vol. 45, no. 2, pp. 312–335, 1985.
- [7] P. L. Goupillaud, "An approach to inverse filtering of near-surface layer effects from seismic records," *Geophys.*, vol. 26, no. 6, pp. 754–760, 1961.
- [8] A. Hasegawa, *Optical Solitons in Fibers*. Springer, 1989.
- [9] M. J. Ablowitz, D. J. Kaup, A. C. Newell, and H. Segur, "The inverse scattering transform – Fourier analysis for nonlinear problems," *Stud. Appl. Math.*, vol. 53, pp. 249–315, 1974.
- [10] E. Agrell, M. Karlsson, A. R. Chraplyvy, D. J. Richardson, P. M. Krummrich, P. Winzer, K. Roberts, J. K. Fischer, S. J. Savory, B. J. Eggleton, M. Secondini, F. R. Kschischang, A. Lord, J. Prat, I. Tomkos, J. E. Bowers, S. Srinivasan, M. Brandt-Pearce, and N. Gisin, "Roadmap of optical communications," *J. Opt.*, vol. 18, no. 6, 2016.
- [11] M. I. Yousefi and F. R. Kschischang, "Information transmission using the nonlinear Fourier transform, Parts I–III," *IEEE Trans. Inf. Theory*, vol. 60, pp. 4312–4369, July 2014.
- [12] E. G. Turitsyna and S. K. Turitsyn, "Digital signal processing based on inverse scattering transform," *Optics Lett.*, vol. 38, no. 20, pp. 4186–4188, 2013.
- [13] J. E. Prilepsky, S. A. Derevyanko, and S. K. Turitsyn, "Nonlinear spectral management: Linearization of the lossless fiber channel," *Optics Express*, vol. 21, no. 20, pp. 24344–24367, 2013.
- [14] J. E. Prilepsky, S. A. Derevyanko, K. J. Blow, I. Gabitov, and S. K. Turitsyn, "Nonlinear inverse synthesis and eigenvalue division multiplexing in optical fiber channels," *Phys. Rev. Lett.*, vol. 113, July 2014. article no. 013901.
- [15] H. Terauchi and A. Maruta, "Eigenvalue modulated optical transmission system based on digital coherent technology," in *Proc. OptoElectron. Commun. Conf/Int. Conf. Photo. Switch. (OECC/PS)*, (Kyoto, Japan), June 2013.
- [16] S. Wahls, S. T. Le, J. E. Prilepsky, H. V. Poor, and S. K. Turitsyn, "Digital backpropagation in the nonlinear Fourier domain," in *Proc. IEEE Wksp. Adv. Signal Process. Adv. Wireless Commun. (SPAWC)*, (Stockholm, Sweden), pp. 445–449, June 2015.
- [17] S. Hari, M. I. Yousefi, and F. R. Kschischang, "Multieigenvalue communication," *J. Lightwave Technol.*, vol. 34, pp. 3110–3117, 2016.
- [18] A. Hasegawa and T. Nyu, "Eigenvalue communication," *J. Lightwave Technol.*, vol. 11, pp. 395–399, Mar. 1993.
- [19] H. Terauchi, Y. Matsuda, A. Toyota, and A. Maruta, "Noise tolerance of eigenvalue modulated optical transmission system based on digital coherent technology," in *Proc. OptoElectron. Commun. Conf/Aust. Conf. Optical Fiber Technol. (OECC/AOFT)*, (Melbourne, Australia), pp. 778–780, July 2014.
- [20] H. Bülow, "Experimental demonstration of optical signal detection using nonlinear Fourier transform," *J. Lightwave Technol.*, vol. 33, no. 7, pp. 1433–1439, 2015.
- [21] Z. Dong, S. Hari, T. Gui, K. Zhong, M. I. Yousefi, C. Lu, P.-K. Wai, F. Kschischang, and A. Lau, "Nonlinear frequency division multiplexed transmissions based on NFT," *IEEE Photonics Lett.*, vol. 27, no. 15, pp. 1621–1623, 2015.
- [22] S. Le, I. Phillips, J. Prilepsky, P. Harper, A. Ellis, and S. Turitsyn, "Demonstration of nonlinear inverse synthesis transmission over transcoherence distances," *J. Lightwave Technol.*, vol. 34, no. 10, 2016.
- [23] S. Wahls and H. V. Poor, "Introducing the fast nonlinear Fourier transform," in *Proc. IEEE Int. Conf. Acoust. Speech Signal Process. (ICASSP)*, (Vancouver, Canada), pp. 5780–5784, May 2013.
- [24] S. Wahls and H. V. Poor, "Fast numerical nonlinear Fourier transforms," *IEEE Trans. Inf. Theory*, vol. 61, pp. 6957–6974, Dec. 2015.
- [25] V. Vaibhav and S. Wahls, "Multipoint Newton-type nonlinear Fourier transform for detecting multi-solitons," in *Proc. OSA Opt. Fiber Conf. (OFC)*, (Anaheim, CA), Mar. 2016. Submitted for publication.
- [26] S. Wahls and H. V. Poor, "Fast inverse nonlinear Fourier transform for generating multi-solitons in optical fiber," in *Proc. IEEE Int. Symp. Inf. Theory (ISIT)*, (Hong Kong, China), pp. 1676–1680, June 2015.
- [27] S. Wahls and V. Vaibhav, "Fast generation of multi-solitons using the Darboux transform," in *Munich Wksp. Inf. Theory Optical Fiber (MIO)*, Tech. Univ. Munich, Inst. Commun. Eng., Dec. 2015. Oral presentation. Slides: <http://bit.ly/2dD61Bh>.

- [28] M. I. Yousefi and X. Yangzhang, "Linear and nonlinear frequency-division multiplexing." Preprint, May 2016. arXiv:1603.04389 [cs.IT].
- [29] A. Buryak, J. Bland-Hawthorn, and V. Steblina, "Comparison of inverse scattering algorithms for designing ultrabroadband fibre Bragg gratings," *Optics Express*, vol. 17, no. 3, pp. 1995–2004, 2009.
- [30] S. T. Le, J. E. Prilepsky, and S. K. Turitsyn, "Nonlinear inverse synthesis for high spectral efficiency transmission in optical fibers," *Optics Express*, vol. 22, pp. 26720–26741, Nov. 2014.
- [31] S. T. Le, J. E. Prilepsky, P. Rosa, J. D. Ania-Castanon, and S. K. Turitsyn, "Nonlinear inverse synthesis for optical links with distributed Raman amplification," *J. Lightwave Technol.*, vol. 34, no. 8, pp. 1778–1786, 2016.
- [32] S. T. Le, S. Wahls, D. Lavery, J. E. Prilepsky, and S. K. Turitsyn, "Reduced complexity nonlinear inverse synthesis for nonlinearity compensation in optical fiber links," in *Proc. Conf. on Lasers & Electro-Optics/Europe (CLEO/EU)*, (Munich, Germany), June 2015.
- [33] S. Blanes, F. Casas, J. A. Oteo, and J. Ros, "The Magnus expansion and some of its applications," *Phys. Rep.*, vol. 470, pp. 151–238, 2009.
- [34] S. Burtsev, R. Camassa, and I. Timofeyev, "Numerical algorithms for the direct spectral transform with applications to nonlinear Schrödinger type systems," *J. Comput. Phys.*, vol. 147, pp. 166–186, Nov. 1998.
- [35] E. Hairer, C. Lubich, and G. Wanner, *Geometric Numerical Integration*. Springer, 2002.
- [36] G. Boffetta and A. R. Osborne, "Computation of the direct scattering transform for the nonlinear Schroedinger equation," *J. Comput. Phys.*, vol. 102, pp. 252–264, Oct. 1992.
- [37] M. Yamada and K. Sakuda, "Analysis of almost-periodic distributed feedback slab waveguides via a fundamental matrix approach," *Appl. Optics*, vol. 26, no. 16, pp. 3474–3478, 1987.
- [38] D. Chang and J. C. Light, "Exponential solution of the Schrödinger equation: Potential scattering," *J. Chem. Phys.*, vol. 50, no. 6, pp. 2517–2525, 1969.
- [39] L. Thylen and D. Yevick, "Beam propagation method in anisotropic media," vol. 21, no. 15, pp. 2751–2754, 1982.
- [40] C. Moler and C. Van Loan, "Nineteen dubious ways to compute the exponential of a matrix, twenty-five years later," *SIAM Review*, vol. 45, no. 1, pp. 3–49, 2003.
- [41] D. S. Bernstein and W. So, "Some explicit formulas for the matrix exponential," *IEEE Trans. Automat. Control*, vol. 38, no. 8, pp. 1228–1232, 1993.
- [42] M. J. Ablowitz and J. F. Ladik, "A nonlinear difference scheme and inverse scattering," *Stud. Appl. Math.*, vol. 55, pp. 213–229, Sept. 1976.
- [43] D. W. McLaughlin and C. M. Schober, "Chaotic and homoclinic behavior for numerical discretizations of the nonlinear Schrödinger equation," *Physica D*, vol. 57, pp. 447–465, Aug. 1992.
- [44] R. Feced, M. N. Zervas, and M. A. Muriel, "An efficient inverse scattering algorithm for the design of nonuniform fiber Bragg gratings," *IEEE J. Quant. Electron.*, vol. 35, pp. 1105–1115, Aug. 1999.
- [45] M. J. Ablowitz and J. F. Ladik, "Nonlinear differential-difference equations and Fourier analysis," *J. Math. Phys.*, vol. 17, pp. 1011–1018, June 1976.
- [46] S. Wahls and H. V. Poor, "Inverse nonlinear Fourier transforms via interpolation: The Ablowitz-Ladik case," in *Proc. Int. Symp. Math. Theory Netw. Syst. (MTNS)*, (Groningen, The Netherlands), pp. 1848–1855, July 2014.
- [47] G.-H. Song and S.-Y. Shin, "Design of corrugated waveguide filters by the Gel'fand-Levitan-Marchenko inverse-scattering method," *J. Opt. Soc. Am. A*, vol. 2, pp. 1905–1915, Nov. 1985.
- [48] O. V. Belai, L. L. Frumin, E. V. Podivilov, and D. A. Shapiro, "Efficient numerical method of the fiber Bragg grating synthesis," *J. Opt. Soc. Am. B*, vol. 24, no. 7, pp. 1451–1457, 2007.
- [49] A. Rosenthal and M. Horowitz, "Inverse scattering algorithm for reconstructing strongly reflecting fiber Bragg gratings," *IEEE J. Quant. Electron.*, vol. 39, pp. 1018–1026, Aug. 2003.
- [50] R. Poovendran, J. E. Dorband, and A. E. Yagle, "An algorithm for forward and inverse scattering in time domain," *J. Acoust. Soc.*, vol. 97, pp. 2021–2027, 1995.
- [51] W. K. McClary, "Fast seismic inversion," *Geophysics*, vol. 48, pp. 1371–1372, Oct. 1983.
- [52] J. Skaar and O. H. Waagaard, "Design and characterization of finite-length fiber gratings," *IEEE J. Quant. Electron.*, vol. 39, pp. 1238–1245, Oct. 2003.
- [53] J. K. Brenne and J. Skaar, "Design of grating-assisted codirectional couplers with discrete inverse-scattering algorithms," *J. Lightwave Technol.*, vol. 21, pp. 254–263, Jan. 2003.
- [54] T. Tao and C. Thiele, "Nonlinear Fourier analysis." Lect. Notes IAS Park City Summer School, July 2003. arXiv:1201.5129v1.
- [55] Y.-J. Tsai, *SU(2) Nonlinear Fourier Transform*. Dissertation, UCLA, Los Angeles, CA, 2005. <http://search.proquest.com/docview/305033060>.
- [56] L. Poladian, "Simple grating synthesis algorithm," *Optics Lett.*, vol. 25, no. 11, pp. 787–789, 2000.
- [57] L. Dong and S. Fortier, "Formulation of time-domain algorithm for fiber Bragg grating simulation and reconstruction," *IEEE J. Quant. Electron.*, vol. 40, pp. 1087–1098, Aug. 2004.
- [58] J. Skaar and R. Feced, "Reconstruction of gratings from noisy reflection data," *JOSA A*, vol. 19, no. 11, pp. 2229–2237, 2002.
- [59] A. H. Sayed and T. Kailath, "A survey of spectral factorization methods," *Numer. Linear Algebra Appl.*, vol. 8, pp. 467–496, 2001.
- [60] D. G. Manolakis and V. K. Ingle, *Applied Digital Signal Processing*. Cambridge Univ. Press, 2011.
- [61] B. Dumitrescu, *Positive Trigonometric Polynomials and Signal Processing Applications*. Springer, 2007.
- [62] M. I. Yousefi and F. R. Kschischang, "Information transmission using the nonlinear Fourier transform, Part I: Mathematical tools," *IEEE Trans. Inf. Theory*, vol. 60, pp. 4312–4328, July 2014.
- [63] I. T. Lima, V. S. Grigoryan, M. O'Sullivan, and C. R. Menyuk, "Computational complexity of nonlinear transforms applied to optical communications systems with normal dispersion fibers," in *Proc. IEEE Photonics Conf. (IPC)*, pp. 277–278, Oct. 2015.
- [64] A. Zettl, *Sturm-Liouville Theory*, vol. 121 of *Math. Surveys Monogr.* Providence, RI: Amer. Math. Soc., 2005.
- [65] W. Rudin, *Principles of Mathematical Analysis*. McGraw-Hill, 3rd ed., 1976.